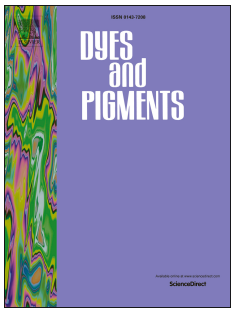

Syntheses and luminescent properties of a series of new lanthanide azelates

Zhiwen Tan, Jian Zhou, Tingting Jiang, Hua-Hong Zou, Lianshe Fu

PII: S0143-7208(20)31335-8

DOI: https://doi.org/10.1016/j.dyepig.2020.108638

Reference: DYPI 108638

To appear in: *Dyes and Pigments*

Received Date: 1 February 2020

Revised Date: 25 May 2020

Accepted Date: 7 June 2020

Please cite this article as: Tan Z, Zhou J, Jiang T, Zou H-H, Fu L, Syntheses and luminescent properties of a series of new lanthanide azelates, *Dyes and Pigments*, https://doi.org/10.1016/j.dyepig.2020.108638.

Zhiwen Tan：Data Curation，Visualization，Software
Jian Zhou：Visualization，Writing - Original Draft，Writing - Review & Editing，Project administration
Tingting Jiang：Data Curation，Visualization
Hua-Hong Zou：Data Curation
Lianshe Fu：Reviewing and Editing

Syntheses and luminescent properties of a series of new lanthanide azelates

Zhiwen Tan, Jian Zhou, Tingting Jiang, Hua-Hong Zou, and Lianshe Fu

Graphical Abstract Legend

This work offers the only example of lanthanide azelates, whose terbium azelate exhibits excellent luminescent sensor targeted for Fe^{3+} ion.

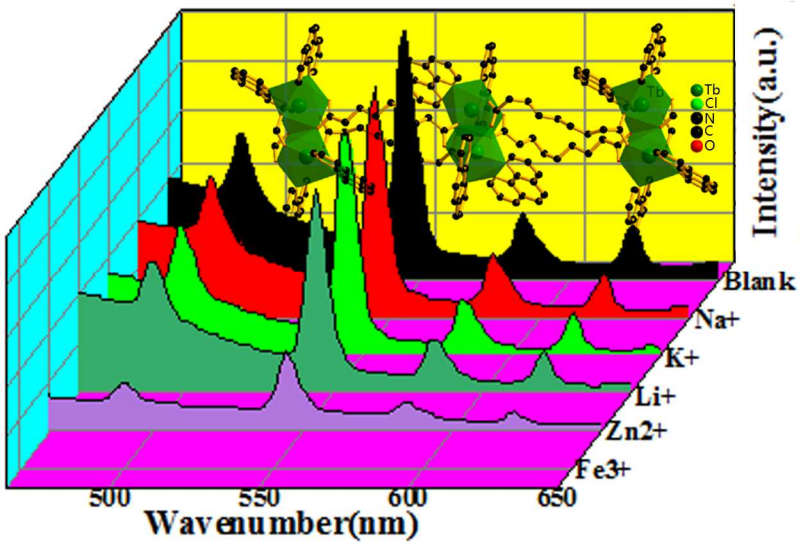

Syntheses and luminescent properties of a series of new lanthanide azelates

Zhiwen Tan,[a] Jian Zhou,[a,*] Tingting Jiang,[a] Hua-Hong Zou,[b,*] and Lianshe Fu[c]

[a]*Chongqing Key Laboratory of inorganic functional materials, College of chemistry, Chongqing normal university, Chongqing, 401331, P.R. China*; [b]*Key Laboratory for the Chemistry and Molecular Engineering of Medicinal Resources (Ministry of Education of China), School of Chemistry and Chemical Engineering of Guangxi Normal University, Guilin 541004, P.R. China.*

[c]*Physics Department and CICECO - Aveiro Institute of Materials, University of Aveiro, 3810-193 Aveiro, Portugal.*

Corresponding author:

Prof. & Dr. Jian Zhou

****

Prof. & Dr. Jian Zhou

College of chemistry,

Chongqing normal university

Chongqing, 401331,
P.R. China
E-mail: Jianzhou888888@163.com

****

Abstract: A series of new lanthanide azelates [Ln(aze)(Haze)(H_2O)]·H_2O {Ln = La (**1a**), Ce (**1b**), Pr (**1c**); H_2aze = azelaic acid}, [$Ln_2(aze)_3(phen)_2$]·H_2O [Ln = Nd (**2a**), Er (**2b**); phen = 1,10-phenanthroline], [Sm(aze)(Haze)(phen)]·$2H_2O$ (**3**), [Gd(aze)$(phen)_2$]·ClO_4 (**4**) and (Hphen)[$Tb_2(aze)_2(phen)_4$]·$3ClO_4$ (**5**) were hydrothermal prepared and structurally characterized.**1a-c** are isostructural and show 3-D framework based on 1-D infinite $[Ln\text{-}O\text{-}Ln]_n$ chain. **2a-b** exhibit sql layer, while **3** displays 1-D chain, where phen ligands locate at both sides of the chain. The Ln^{3+} ions of **4** and **5** are connected by aze^{2-} into two different types of rare cationic 1-D chains. The luminescent investigations show that both **2a** and **2b** exhibit interesting NIR luminescence and **5** displays a good potentiality as a luminescent sensor targeted for Fe^{3+} ion. Of particular interest, lanthanide azelates have not been to date documented, while this work presents the only examples of lanthanide azelates exhibiting luminescent properties. The magnetic properties of some lanthanide azelates were also investigated.

Keywords: Hydrothermal syntheses; Lanthanide azelates; Structure; Luminescent properties.

1 Introduction

Metal coordination polymers (MCPs) have attracted considerable interest, because of their intriguing structural topologies and potential applications in the fields of catalysis, magnetism, sensors, luminescence, ion exchange and the others [1-5]. Among MCPs, lanthanide coordination polymers (Ln-CPs) are regarded as an important class of functional MCPs, due to their unique luminescence properties, such as high color purity, visible color naked eye, and large Stokes shifts [6-9]. Multiple colors including white light emitting materials can be accomplished by adjusting the relative amounts of these Ln^{3+} ions in a material [6-10]. Due to Laporte forbidden f–f transitions of Ln^{3+} ions, Ln-CPs have weak emission intensities and low quantum yields, but suitable π–conjugated aromatic chromophore coordinates to Ln^{3+} ion [11-12], where an energy transfer process occurs from the chromophore excited state to the Ln^{3+} excited state and enhances subsequently emission intensities of the Ln^{3+} ions. Significantly, the brilliant luminescent properties of Ln-CPs make them attractive for promising applications as luminescent

bioassays and optical sensors [13-22].

Fe^{3+} is a ubiquitous ion in human or other animals, because a variety of vital cell functions (such as the formation of haemoglobin and muscle, the transport of oxygen, and the improvement of brain function) are closely related to the specific amount of Fe^{3+} [23-25]. The deficiency or excess of Fe^{3+} can largely affect human health, resulting in hazardous diseases, as exemplified by pathological disorders, anaemia and skin ailments [24-26]. Hence, it is important to rapid and selective detection of the amounts of Fe^{3+}. So far, a few Ln-CPs exhibit the good luminescent sensor for Fe^{3+} [26-33], but the progress in this specific area has not yet reached what is expected, because of the detection sensitivity limited by the luminescent quenching caused *via* cation exchange.

In order to obtain sensitive and selective luminescent sensors, the effective and facile approach for the syntheses of the luminescent Ln-CPs is still the judicious choice of well-designed organic linker with Ln^{3+} ion, which affords varied frameworks. The carboxylate based ligand with the hard O-donor is preferable to link with hard Ln^{3+} ion, resulting in different new extended frameworks based on the versatile binding modes of the carboxylate groups [6-10], while 1,10-phenanthroline (phen) is one of the most widely used chromophores in the design of luminescent lanthanide complexes because it can absorb and efficiently transfer energy to the Ln^{3+} excited states [34-36], It is expected that the combination of the phen and carboxylate based ligands in the same Ln-CPs may generate a new class of materials with novel structures and useful properties. Guided by this idea, we have recently used by combining Ln^{3+} with a mixed phen and organic carboxylic acids to successfully construct a series of lanthanide oxo clusters {$[Ln_8(phen)_2Ge_{12}(\mu_3\text{-}O)_{24}T_{12}(H_2O)_{16}]\cdot 2H_2O$ (Ln = Dy, Er; T = $-CH_2CH_2COO^-$ group], $[Ln_8(phen)_2Ge_{12}(\mu_3\text{-}O)_{24}T_{12}(H_2O)_{16}]\cdot 2phen\cdot 16H_2O$ (Ln = Sm, Eu, Gd) and $[Ho_8(phen)_2Ge_{12}(\mu_3\text{-}O)_{24}T_{12}(H_2O)_{14}]\cdot 2phen\cdot 13H_2O$}[37] and lanthanide coordination polymers {$[Ln(phen)(glu)Cl]_n$ (Ln = Y, Tm; glu = glutarate), $[Ln_2(phen)_2(glu)_3]_n$ (Ln = Ce, Dy, Tb, Ho), $[Sm(phen)(Hpim)(pim)]_n\cdot 1.5nH_2O$ (H_2pim = pimelic acid) and $[Ln(phen)(pim)]_n\cdot nClO_4\cdot nH_2O$ (Ln = Gd, Tb, Er)}[38-40], which exhibit stronger characteristic Ln^{3+} emissions, because they are closely related to the incorporation of phen chromophores into lanthanide oxo cluster or lanthanide coordination polymeric

frameworks. As part of the continuing work in this system, herein we reported the hydrothermal syntheses, structures and properties of a series of new lanthanide azelates [Ln(aze)(Haze)(H_2O)]·H_2O [Ln = La (**1a**), Ce (**1b**), Pr (**1c**)], [Ln_2(aze)$_3$(phen)$_2$]·H_2O [Ln = Nd (**2a**), Er (**2b**)], [Sm(aze)(Haze)(phen)]·$2H_2O$ (**3**), [Gd(aze)(phen)$_2$]·ClO_4 (**4**) and (Hphen)[Tb_2(aze)$_2$(phen)$_4$]·$3ClO_4$ (**5**), whose terbium azelate shows a good potentiality as a luminescent sensor targeted for Fe^{3+}. The azelaic acid (H_2aze), as a typical flexible linker with a –(CH_2–)$_7$ spacer, has a flexible bridging capability for the construction of a diversity of MCPs. As a result, a large number of new varied MCPs based on the combination of the aze^{2-} or $Haze^-$ as organic linkers and d- or ds-block metal ions have been reported [41-53], but no lanthanide azelates have been reported until now to the best of our knowledge, due to synthetic difficulties. Therefore, the present compounds offer the only example of lanthanide azelates containing the longer flexible aze^{2-} or $Haze^-$ ligands.

2 Experimental Sections

2.1 General Remarks

All analytical grade chemicals were obtained commercially and used without further purification. Elemental analyses (C and H) were performed using a PE2400 II elemental analyzer. IR spectra were obtained from a powdered sample pelletized with KBr on an ABB Bomen MB 102 series IR spectrophotometer in the range of 400–4000 cm^{-1}. Room-temperature optical diffuse reflectance spectra of the powdered samples were obtained with a Shimadzu UV-3150 spectrometer. Photoluminescence spectrum and lifetime were performed on an Edinburgh FLS 980 analytical instrument equipped with 450 W xenon lamp and UF900H high-energy microsecond flashlamp as the excitation source. Variable-temperature magnetic susceptibility measurements were carried out in the temperature range of 2–300 K with a Quantum Design MPMS-5 magnetometer. PXRD patterns were obtained using a Bruker D8 Advance XRD diffractometer with Cu Kα radiation (λ = 1.54056 Å).

2.2 Synthesis of [La(aze)(Haze)(H_2O)]·H_2O (**1a**). A mixture of H_2aze (0.0328 g, 0.13 mmol), $LaCl_3$ (0.1035 g, 0.4 mmol) and water (3 mL) was stirred for 20 min, and then the pH value of the mixed solution was adjusted to 6 by ethylenediamine (en) dilute solution (en : H_2O = 1 : 100, V/V). The final mixture was sealed in a 25 mL Teflonlined autoclave and heated at 130 °C for 10 days. After cooling to room temperature slowly, light colorless block crystals were isolated. The

yield of **1a** is 65 % based on $LaCl_3$. Anal. calcd. for **1a**, $C_{18}H_{33}LaO_{10}$, C 39.43 %, H 6.07 %, found: C 38.72 %, H 5.81 %. IR (cm^{-1}): 3477(m), 2929(vs), 2845(s), 1635(s), 1539(vs), 1436(vs), 1341(s), 1271(s), 1194(m), 1093(s), 933(w), 825(s), 774(s).

2.3 Synthesis of [Ce(aze)(Haze)(H_2O)]·H_2O (1b). The colorless crystals of **1b** were prepared similarly from $CeCl_3$ (yield 63% based on $CeCl_3$). Anal. calcd. for **1b**, $C_{18}H_{33}CeO_{10}$, C 39.34 %, H 6.05 %, found: C 39.96 %, H 5.93 %. IR (cm^{-1}): 3349(m), 2935(s), 2858(s), 1657(w), 1513(vs), 1443(vs), 1405(s), 1341(s), 1271(m), 1194(m), 1105(w), 940(w), 844(w), 723(s).

2.4 Synthesis of [Pr(aze)(Haze)(H_2O)]·H_2O (1c). The green crystals of **1c** were prepared similarly from $PrCl_3$ (yield 68% based on $PrCl_3$). Anal. calcd. for **1c**, $C_{18}H_{33}O_{10}Pr$, C 39.28 %, H 6.04 %, found: C 39.74 %, H 5.45 %. IR (cm^{-1}): 3368(s), 2929(vs), 2845(s), 1654(w), 1520(vs), 1450(s), 1411(s), 1341(m), 1265(m), 1227(m), 1093(w), 946(w), 723(s).

2.5 Synthesis of [Nd_2(aze)$_3$(phen)$_2$]·H_2O (2a). A mixture of H_2aze (0.0457 g, 0.24 mmol), phen (0.0817 g, 0.4 mmol), Nd_2O_3 (0.1080 g, 0.32 mmol) and water (3 mL) was stirred for 10 min, and then the pH value of the mixed solution was adjusted to 2 by HCl (12 mol/L). The final mixture was sealed in a 25 mL Teflonlined autoclave and heated at 120 °C for 10 days. After cooling to room temperature slowly, pink block crystals were isolated. The yield of **2a** is 45 % based on Nd_2O_3. Anal. calcd. for **2a**, $C_{51}H_{60}N_4Nd_2O_{13}$, C 49.98 %, H 4.93 %, N 4.57 %, found: C 49.82 %, H 4.89 %, N 4.64 %. IR (cm^{-1}): 3362(m), 3078(vw), 2935(s), 2858(s), 1644(w), 1584(s), 1520(vs), 1550(vs), 1405(s), 1347(w), 1309(w), 1265(w), 1194(w), 1099(w), 844(s), 723(s), 627(w).

2.6 Synthesis of [Er_2(aze)$_3$(phen)$_2$]·H_2O (2b). The pink prism-like crystals of **2b** were prepared by a similar method used in the synthesis of the crystals of **2a** except that Nd_2O_3 was replaced by Er_2O_3 (yield 47 %, based on Er_2O_3). Anal. calcd. for **2b**, $C_{51}H_{60}Er_2N_4O_{13}$, C 48.17 %, H 4.76 %, N 4.41 %, found: C 48.27 %, H 4.81 %, N 4.48 %. IR (cm^{-1}): 3356(s), 3058(vw), 2929(vs), 2845(s), 1551(vs), 1469(m), 1450(m), 1417(s), 1316(w), 1213(w), 1093(s), 946(s), 844(s), 729(s), 691(m), 589(w).

2.7 Synthesis of [Sm(aze)(Haze)(phen)]·2H_2O (3). A mixture of H_2aze (0.0576 g, 0.3 mmol), phen (0.0750 g, 0.38 mmol), Sm_2O_3 (0.0897 g, 0.25 mmol) and water (3 mL) was stirred for 10 min, and then the pH value of the mixed solution was adjusted to 2 by HCl (12 mol/L). The final mixture was sealed in a 25 mL Teflonlined autoclave and heated at 120 °C for 10 days. After cooling to room temperature slowly, light yellow block crystals were isolated. The yield of **3** is

44 % based on Sm_2O_3. Anal. calcd. for **3**, $C_{30}H_{41}N_2O_{10}Sm$, C 48.69 %, H 5.58 %, N 3.79 %, found: C 48.38 %, H 4.98 %, N 4.22 %. IR (cm^{-1}): 3445(m), 3078(vw), 2935(m), 2845(m), 1584(vs), 1545(vs), 1524(vs), 1341(w), 1309(m), 1093(m), 844(s), 736(s), 633(w).

2.8 Synthesis of [Gd(aze)(phen)$_2$]·ClO$_4$ (4). A mixture of H_2aze (0.0406 g, 0.21 mmol), phen (0.0779 g, 0.39 mmol), Gd_2O_3 (0.1140 g, 0.32 mmol) and water (3 mL) was stirred for 10 min, and then the pH value of the mixed solution was adjusted to 2 by $HClO_4$ (12 mol/L). The final mixture was sealed in a 25 mL Teflonlined autoclave and heated at 120 ℃ for 10 days. After cooling to room temperature slowly, light yellow block crystals were isolated. The yield of **4** is 43 % based on Gd_2O_3. Anal. calcd. for **2**, $C_{33}H_{30}ClGdN_4O_8$, C 49.34 %, H 3.76 %, N 6.97 %, found: C 49.03 %, H 3.64 %, N 6.18 %. IR (cm^{-1}): 3413(m), 3068(w), 2929(s), 2852(s), 1589(vs), 1520(m), 1424(s), 1335(m), 1150(w), 1086(vs), 850(s), 767(m), 736(s), 627(s).

2.9 Synthesis of (Hphen)[Tb$_2$(aze)$_2$(phen)$_4$]·3ClO$_4$ (5). A mixture of H_2aze (0.0465 g, 0.24 mmol), phen (0.0817 g, 0.41 mmol), Tb_4O_7 (0.0770 g, 0.10 mmol) and water (3 mL) was stirred for 10 min, and then the pH value of the mixed solution was adjusted to 2 by $HClO_4$ (12 mol/L). The final mixture was sealed in a 25 mL Teflonlined autoclave and heated at 120 ℃ for 10 days. After cooling to room temperature slowly, brown block crystals were isolated. The yield of **5** is 45 % based on Tb_4O_7. Anal. calcd. for **5**, $C_{78}H_{71}Cl_3N_{10}O_{21}Tb_2$, C 49.08 %, H 3.75 %, N 7.34 %, found: C 49.15 %, H 3.65 %, N 7.25 %. IR (cm^{-1}): 3445(m), 3075(w), 2929(m), 2852(m), 1589(m), 1551(s), 1462(m), 1417(s), 1335(w), 1099(vs), 850(m), 723(s), 621(m).

2.10 Crystal Structure Determinations

Single-crystal X-ray diffraction data for all compounds were collected on a Bruker diffractometer-SMART-APEX II using a ω-scan method with graphite monochromated Mo Kα radiation (λ = 0.71073 Å). Data reduction and absorption corrections were performed using the SAINT and SADABS software packages, respectively [54]. The structures of all compounds were solved by direct methods and refined by full-matrix least-squares methods on F^2 using the SHELXL-2018 program package [55]. The C24-C28 atoms in **2a-b** are disordered over site occupation factors of 0.5/0.5, while O1w atoms have occupancy of 0.5. For **5**, the ClO_4^- ions and aze^{2-} ligands are disordered. Positions of H atoms attached to the C atoms were geometrically placed and H atoms were refined isotropically as a riding mode using the default SHELXTL parameters. A summary of crystallographic data is listed in Table 1. The CCDC reference numbers

are 1963279-1963286.

3 Results and Discussion

3.1 Crystal structure

Description of [Ln(aze)(Haze)(H_2O)]·H_2O [Ln = La (1a), Ce (1b), Pr (1c)]. **1a-c** are isostructural. Hence only **1a** is discussed here in detail. **1a** crystallizes in the monoclinic space group $P2_1/n$ and its asymmetric unit has one La^{3+} ion, one $Haze^-$, one aze^{2-}, one coordinated H_2O molecule and one free H_2O molecule (Fig. 1a). The central $(-CH_2-)_7$ chain of aze^{2-} and $Haze^-$adopts a nearly extended conformation. The central La^{3+} ion is ten-coordinated environment (Fig. 1b) with three O atoms of three $Haze^-$, six O atoms of four aze^{2-} ligands and one coordinated water molecule. The La-O bond distances vary from 2.4655(16) to 2.7578(16) Å lying within the range of the distances in other La^{2+} complexes [56]. $Haze^-$ and aze^{2-} show different link modes. aze^{2-} has two chelating-*anti* –COO ends (Fig. S1a), while $Haze^-$ has one *syn* and one *anti–anti* –COO ends (Fig. S1b). The adjacent La^{3+} ions are bridged by chelating-*anti* –COO group of aze^{2-} and *anti–anti* –COO group of $Haze^-$, resulting in a 1-D infinite chain with La···La distances of 4.314-4.499 Å. These 1-D infinite chains (Fig. 1c) are further interlinked by *syn*–COO group of $Haze^-$ and chelating-*anti* –COO group of aze^{2-}, forming a 3-D network structure with 1-D channels that are occupied by lattice water molecules (Figs. 1d-e).

---- Insert Fig. 1 here ---

Description of [$Ln_2(aze)_3(phen)_2$]·H_2O [Ln = Nd (2a), Er (2b)]. **2a-b** have the general formula $[Ln_2(aze)_3(phen)_2]\cdot H_2O$ and are isostructural. So only **2a** is discussed here in detail. The crystal structure of **2a** consists of 2-D $[Nd_2(aze)_3(phen)_2]_n$ layers and free H_2O molecules. Each Nd^{3+} ion adopts a distorted tricapped trigonal prism (Fig. 2a) with seven O atoms of five aze^{2-} ligands and two N atoms from a chelating phen ligand. The Nd–O/N bond distances vary from 2.392(4) to 2.679(5) Å lying within the range of the distances in other Nd^{2+} compounds [57-58]. One central $(-CH_2-)_7$ chain of aze^{2-} shows a S-like conformation, the other displays a nearly extended conformation. aze^{2-} exhibits different link modes with distinct crystal engineering functions. One type has two chelating-*anti* –COO ends (Fig. S1c), and another has one chelating and one *anti–anti* –COO ends (Fig. S1d). Two $[Nd(phen)]^{3+}$ groups are bridged by two chelating-*anti* –COO and two *anti–anti* –COO groups, forming centrosymmetric Nd_2 dimer with a Nd···Nd distance of 3.997 Å. These Nd_2 dimers are interconnected *via* aze^{2-} ligands to give a 2-D

layer parallel to the ac plane (Fig. 2b). The topology of the 2-D layer in **2a** can be simplified by considering the Nd_2 dimers and aze^{2-} ligands as nodes and linkers, respectively. As a result, a 2-D layer structure of sql topological net with single and double edges is formed (Fig.2c). The Schläfli symbol of this net is $4^4 \cdot 6^2$. There are π–π stacking interactions of phen ligands within the $[Nd_2(aze)_3(phen)_2]_n$ layer, and centroid-to-centroid distance of adjacent phen ligands is 3.828 Å (Fig.2d), which plays an important role in stabilizing **2a** in the solid state. These layers are stacked in -AAA- fashion (Fig.2e) and no π–π stacking interactions are observed between the $[Nd_2(aze)_3(phen)_2]_n$ layers.

---- Insert Fig. 2 here ---

Description of $[Sm(aze)(Haze)(phen)]\cdot 2H_2O$ (3). The crystal structure of **3** contains 1-D neutral $[Sm(aze)(Haze)(phen)]_n$ chain and free H_2O molecules. The coordination geometry of Sm^{3+} ion can be described as a distorted topcapped square antiprism comprised of five O atoms of three $Haze^-$ ligands, two O atoms from two aze^{2-} ligands and two N atoms of one phen ligand (Fig. 3a). The Sm–O/N bond distances are in the range of 2.3654(17)-2.7225(18) Å, compared with corresponding values in other Sm^{3+} complexes [59-60]. $Haze^-$ ligand shows chelating coordination mode (Fig. S1e), and aze^{2-} ligand has one chelating and one *anti–anti* –COO ends (Fig. S1d). The adjacent [Sm(Haze)(phen)] groups are bridged by aze^{2-} ligands to generate a 1-D neutral $[Sm(aze)(Haze)(phen)]_n$ chain (Fig. 3b). $Haze^-$ and phen ligands with chelating mode coordinate to Sm^{3+} ions and are regularly located at both sides of the chain. These chains are further interacted by π-π aromatic stacking interactions between adjacent phen ligands with centroid-to-centroid distances of 3.817 Å (Fig. 3c), forming a 2-D layer (Fig. 3d). Then 2-D layers are arranged in a parallel manner, resulting in a 3-D supramolecular network structure with 1-D channels, which are filled by free H_2O molecules.

---- Insert Fig. 3 here ---

Description of $[Gd(aze)(phen)_2]\cdot ClO_4$ (4) and (Hphen)-$[Tb_2(aze)_2(phen)_4]\cdot 3ClO_4$ (5). The asymmetric unit of **4** contains one Gd^{3+} ion, one aze^{2-} ligand, two phen ligands and one ClO_4^- anion (Fig. S4). The central $(-CH_2-)_7$ chain of aze^{2-} in **4** shows a curved configuration, as evidenced by torsion angles deviating from 180 °. The aze^{2-} ligand has two *anti–anti* –COO ends connecting neighboring $[Gd(phen)_2]^{3+}$ cations to generate a 1-D cationic $[Gd(aze)(phen)_2^+]_n$ chain (Fig. 4a). These chains are arranged in a parallel manner and interacted *via* π–π stacking

interactions of phen ligands with centroid-to-centroid distance of 3.656 Å, resulting in a pseudo-layered arrangement parallel to the (001) plane (Fig. 4c). These pseudo-layers are further stacked in -ABA- fashion along the c-axis, leading to a 3-D supramolecular network structure (Fig. 4e).

---- Insert Fig. 4 here ---

The crystal structure of **5** consists of protonated $Hphen^{+}$ ion, 1-D cationic $[Tb(aze)(phen)_2^{+}]_n$ chain and free ClO_4^{-} anions. There are two kinds of coordination modes of aze^{2-} ligands in **5**. One has two *anti–anti* –COO ends (Fig. S1f), while the other has two chelating-*anti* –COO ends (Fig. S1c). The adjacent Tb^{3+} ions are bridged by two types of aze^{2-} ligands to form 1-D infinite $[Tb(aze)(phen)_2^{+}]_n$ chains with a shortest Tb···Tb distance of 3.896 Å(Fig. 4b). These chains are aligned in an antiparallel fashion and connected by π–π stacking interactions of phen ligands with centroid-to-centroid distances of 3.591-3.891 Å, forming a pseudo-layered arrangement (Fig. 4d). The adjacent layers are stacked in an -AAA- sequence along the c axis, and the interlayer distance is estimated to be 13.01 Å (Fig. 4f). The free protonated $Hphen^{+}$ ions and ClO_4^{-} anions are located at the interlayer spaces.

Although **4** and **5** contain same formula $[Ln(aze)(phen)_2^{+}]_n$, they display completely different structures. The first is that different coordination modes of aze^{2-} ligands: **4** has only type of aze^{2-} ligand, and **5** has two types of aze^{2-} ligands. The second is different packing of 1-D $[Ln(aze)(phen)_2^{+}]_n$ chains: the pseudo-layer based on the parallel arrangement of 1-D chains in **4** is stacked in an -ABA- sequence, but the pseudo-layer constructed by the antiparallel arrangement of 1-D chains in **5** is stacked in an -AAA- sequence. Moreover, although some MCPs built up from the linkages of transition metal ions and aze^{2-} or $Haze^{-}$ ligands have been reported, they usually show the neutral extended frameworks. Notably, cationic extended frameworks of MCPs have not been obtained until now to the best of our knowledge. Therefore, **4** and **5** provide the only examples of cationic metal azelate frameworks.

3.2 Synthetic aspects and Spectroscopic properties

A series of lanthanide azelates have been obtained under hydrothermal conditions in the presence of different acid or alkali reagents. Originally, the pH value of mixed solution was adjusted to 6 by ethylenediamine, resulting in the formation of 3-D neutral frameworks $[Ln(aze)(Haze)(H_2O)]\cdot H_2O$ [Ln = La (**1a**), Ce (**1b**), Pr (**1c**)] with two different types of ligand

binding modes, whose positive charge of Ln^{3+} ions is compensated by one aze^{2-} and one $Haze^{-}$. To consider the high-vibrational O-H oscillator of H_2O molecule tending to quench photoluminescence of the Ln^{3+} ions, phen chromophore, which can prevent the Ln^{3+} ion from the H_2O molecules, was introduced into the reaction system and the pH value was adjusted to 2 by HCl, leading to the 2-D neutral layers $[Ln_2(aze)_3(phen)_2]\cdot H_2O$ [Ln = Nd (**2a**), Er (**2b**)]. When the quantity of H_2aze ligand was slightly increased, other parameters remained unchanged, new 1-D chain $[Sm(aze)\text{-}(Haze)(phen)]\cdot 2H_2O$ (**3**) with doubly and singly deprotonated ligands is formed. When HCl was replaced by $HClO_4$ under similar condition to result in another type of 1-D chain $[Gd(aze)(phen)_2]\cdot ClO_4$ (**4**), where ClO_4^- anion was incorporated into the final structure and compensates the positive charge of $[Gd(aze)(phen)_2^+]_n$. Under similar conditions, phen was slightly increased, leading to another new 1-D chain $(Hphen)[Tb_2(aze)_2(phen)_4]\cdot 3ClO_4$ (**5**) containing protonated $Hphen^+$ cation. Notably, phen was introduced into the lanthanide azelate framework, it acting as a terminating group prevents further connections, resulting in the low dimensional structures, for instance, **2a-b** show 2-D layer, while **3-5** exhibit 1-D chain.

--- Insert Fig. 5 here ---

Their IR spectra (Fig. S5) exhibit the characteristic $\nu_{C=O/C-O}$ asymmetric stretching (1513–1657 cm^{-1}) and $\nu_{C=O/C-O}$ symmetric stretching (1335–1469 cm^{-1}) of carboxylate groups. The broad bands at 3345–3477 cm^{-1} can be assigned to $\nu_{O\text{-}H}$ stretching of coordinated H_2O or free H_2O molecules. For **2a-b** and **3-5**, the weak bands at 3058–3078 cm^{-1} belong to the ν_{C-H} stretching of phen ligand, but no similar bands have been observed in **1a-c**. For **4** and **5**, the strong band at about 1097 cm^{-1} is characteristic of ClO_4^- ion. UV/Vis absorption spectra of all compounds (Fig. 5 and Fig. S6) were calculated from the data of diffuse reflectance by using the Kubelka–Munk function [61]. The strong absorptions in the ultraviolet region can be assigned to the O/N→Ln charge transfers of all compounds. In addition, there are some absorption characteristics of the f–f transitions of Ln^{3+} ions {442 nm ($^3H_4\rightarrow{}^3P_2$), 467 nm ($^3H_4\rightarrow{}^3P_1$), 483 nm ($^3H_4\rightarrow{}^3P_0$) and 590 ($^3H_4\rightarrow{}^1D_2$) for Pr^{3+}, and 522 nm ($^4I_{9/2}\rightarrow{}^4G_{7/2}+{}^2K_{13/2}$), 581 nm ($^4I_{9/2}\rightarrow{}^4G_{5/2}+{}^2G_{7/2}$), 742 nm ($^4I_{9/2}\rightarrow{}^4S_{3/2}+{}^4F_{7/2}$), 800 nm ($^4I_{9/2}\rightarrow{}^4F_{5/2}+{}^2H_{9/2}$) and 871 nm ($^4I_{9/2}\rightarrow{}^4F_{3/2}$) for Nd^{3+}, and 400 nm ($^6H_{5/2}\rightarrow{}^4F_{7/2}$) and 1096 nm ($^6H_{5/2}\rightarrow{}^6F_{9/2}$) for Sm^{3+}, and 378 nm ($^4I_{15/2}\rightarrow{}^2H_{9/2}$), 406 nm ($^4I_{15/2}\rightarrow{}^4F_{3/2}$), 447 nm ($^4I_{15/2}\rightarrow{}^4F_{5/2}$), 488 nm ($^4I_{15/2}\rightarrow{}^4F_{7/2}$), 521 nm ($^4I_{15/2}\rightarrow{}^2H_{11/2}$), 653 nm ($^4I_{15/2}\rightarrow{}^4F_{9/2}$) and 975 nm ($^4I_{15/2}\rightarrow{}^4F_{11/2}$) for Er^{3+}}, which are in agreement with the UV-vis spectra of other lanthanide complexes [62-64].

--- Insert Fig. 6 here ---

Ln-CPs usually show promising luminescent properties due to the effective intramolecular energy transfer from the organic ligand to lanthanide ions. For **2a-b**, since the energy levels of Nd^{3+} and Er^{3+} ions are very close to one another, the emissions are often in the infrared region (Figs. 6a-b) [65]. Upon excitation at 345 nm in the UV region, **2a** exhibits the typical f-f transition at 1061 and 1340 nm corresponding to $^4F_{3/2}\rightarrow{}^4I_{11/2}$ and $^4F_{3/2}\rightarrow{}^4I_{13/2}$ transitions of Nd^{3+} ions, while **2b** shows a broad band from 1450 to 1650 with the maximum emission wavelength at 1523 nm originating from the transition of $^4I_{13/2}\rightarrow{}^4I_{15/2}$ of Er^{3+} ions. This suggests that the ligands can sensitize the emission of Nd^{3+} and Er^{3+}ions by UV radiation. The lifetime-decay curves of **2a** and **2b** on monitoring the emission at λ = 1061 nm (**2a**, Fig. S7) and 1523 nm (**2b**, Fig. S8) obey a second-order exponential function. The resulting lifetime values are τ_1 = 1.51 µs (**2a**, 56.77 %) and 4.13 µs (**2b**, 53.61 %), τ_2 = 12.35 µs (**2a**, 43.23 %) and 18.33 µs (**2b**, 46.39 %). The average decay time (τ*) can be determined by using the formula $\tau^* = (A_1\tau_1^2 + A_2\tau_2^2)/(A_1\tau_1 + A_2\tau_2)$ [66], thus their average lifetimes are calculated to be 5.66 µs for **2a** and 9.23 µs for **2b**. The quantum efficiencies for **2a** and **2b** are 17.18 % and 18.37 %, respectively.

Fig. 6c presents the emission spectrum of **3** with 378 nm excitation wavelength. **3** shows three emission transitions that are assigned to $^4G_{5/2}\rightarrow{}^6H_{5/2}$ (561 nm), $^4G_{5/2}\rightarrow{}^6H_{7/2}$ (596 nm), and $^4G_{5/2}\rightarrow{}^6H_{9/2}$ (643 nm) optical transitions. Among them, the transition $^4G_{5/2}\rightarrow{}^6H_{7/2}$ has shown a strong orange emission. Generally, the greater the intensity of the electric dipole (ED) transition, the more the asymmetry nature [67]. The $^4G_{5/2}\rightarrow{}^6H_{9/2}$ (ED) transition of Sm^{3+} ion in **3** is more intense than $^4G_{5/2}\rightarrow{}^6H_{5/2}$ magnetic dipole transition, specifying the asymmetric nature of a distorted topcapped square antiprism (SmN_2O_7). The luminescence decay curve of **3** related to the $^4G_{5/2}\rightarrow{}^6H_{7/2}$ emission is shown in Fig. S9. The decay curve can be well fitted with a second-order exponential function. The fitting lifetimes were τ_1 = 2.32 µs (38.91 %) and τ_2 = 9.76 µs (61.09 %) and the average lifetime was calculated to be τ* = 6.91 µs. Upon excitation at 275 nm, **4** shows a sharp line peak at about 312 nm and a broad emission from 350 to 540 nm with maximum emission wavelength of 396 nm (Fig. S10). The emission peak at 312 nm is assigned to the transition $^6P_{7/2}\rightarrow{}^8S_{7/2}$ for Gd^{3+} [68], and the strong emission at 396 nm originates from the phen ligand, similar to the emission of pure phen ligand (Fig. S11) [37].

For **5**, upon excitation at the most intensive wavelength 271 nm, the emission spectrum (Fig.

6d) exhibits four strong emission bands at 489, 545, 584 and 621 nm corresponding to $^5D_4 \rightarrow {}^7F_J$ (J=6, 5, 4, 3), and three weak bands located at 648, 667 and 679 nm arising from the $^5D_4 \rightarrow {}^7F_J$ (J=2, 1, 0), respectively, with the green emission of $^5D_4 \rightarrow {}^7F_5$ as the dominant band. The phen ligand can give an emission in the UV and blue regions (Fig. S11). Nearly no emission from the phen ligand is detected, indicating an efficient energy transfer from the ligand to Tb^{3+} ions, which supports the idea that the quenching of the phen-related emission can be attributed to ligand-to-Tb^{3+} energy transfer. The luminescence decay curve of **5** related to the $^5D_4 \rightarrow {}^7F_5$ emission is shown in Fig. S12. The decay curve is a bi-exponential function, so resulting in τ_1 = 2.16 μs (8.72 %), τ_2 = 496.85 μs (91.28 %), and τ^* = 0.50 ms. No emissions of **1a-c** are observed in the visible region, which could be related to the absence of phen chromophore.

--- Insert Fig. 7 here ---

3.3 Luminescent sensor

To consider the free $Hphen^+$ ion with Lewis basic N-donor and the bright green luminescence of **5**, the luminescent detection for different metal ions was assessed. 1 mg of **5** was dispersed into 5 mL of an aqueous solution (0.1 M) containing different MCl_x (M = Li^+, Na^+, K^+, Zn^{2+}, Fe^{3+}), forming a suspension solution by an ultrasound method, the characteristic emissions of Tb^{3+} ions were measured. As clearly seen from Figs. 7a-b, Li^+, Na^+, K^+ and Zn^{2+} decreased the luminescent intensity of the sample to a different extent, while the luminescent emission of **5** was severely quenched in the $FeCl_3$ suspension. The possible reason is that binding of Fe^{3+} to the N atoms of free $Hphen^+$ ion leads to luminescent quenching of **5**, and the paramagnetic effect caused by the unpaired d-electrons in Fe^{3+} promotes dissipation of the excited state energy in a nonradiative process [27]. This luminescent quenching affected by Fe^{3+} implies the potentiality of **5** for a high selectivity and sensitivity to Fe^{3+} ions.

In order to further investigate the relationship between the quenching effect of **5** and Fe^{3+} ions concentration, the following experiments were carried out. 1 mg of **5** was dispersed into 5 mL of different concentrations (mmol/L) of $FeCl_3$ aqueous solutions (pH = 5), and oscillated for 2 min by ultrasonic waves to form uniform dispersion, and then the emission of Tb^{3+} ion was performed (Fig. 7c). The luminescent intensity *vs* [Fe^{3+}] plot can be curve-fitted into $I_0/I = K_{SV}[Fe^{3+}] + 0.93$ with a good linear correlation (R^2 = 0.996, Fig. 7d), which is very close to the Stern−Volmer equation: $I_0/I = K_{SV}[M] + 1$, where I_0 and I are the luminescent intensity before and after metal ion

incorporation, respectively, K_{SV} is the Stern−Volmer constant, and [M] is the metal ion molar concentration. The value of K_{SV} for Fe^{3+} is calculated to be 6.47×10^3 L/mol, which is compared with those of other well-designed Fe^{3+} luminescent sensors (typical K_{SV} in the range of 4.1×10^3~1.30×10^4) [26-32]. To investigate the stability of **5** after Fe^{3+} solution exposition, **5** was soaked in a $FeCl_3$ aqueous solution (0.1 mol/L) for 12 h, followed by filtration and rinse with deionized water. PXRD (Fig. S13) indicated that its structure in Fe^{3+} solution remains intact. Meanwhile, the luminescence intensity of the recycled **5** is well consistent with the simulated one from **5**, and two runs were made (Fig. S14). This result shows that **5** can be reused.

--- Insert Fig. 8 here ---

3.4 Magnetic properties

The magnetic susceptibilities of **1b-c** and **2-5** were measured in the temperature range 2–300 K under an applied magnetic field of 1 kOe (Fig. 8). For **1a-b**, the $\chi_M T$ values at 300 K are 0.83 $cm^3\cdot mol^{-1}\cdot K$ for **1b**, and 1.57 $cm^3\cdot mol^{-1}\cdot K$ for **1c**, which are close to the expected value of one non-interacting Ln^{3+} ion (0.80 $cm^3\cdot mol^{-1}\cdot K$ for Ce^{3+}, $^2F_{5/2}$, S = 1/2, L = 3, g = 6/7, J = 5/2, and 1.60 $cm^3\cdot mol^{-1}\cdot K$ for Pr^{3+}, $^3H_4$, S = 1, L = 5, g = 4/5, J = 4) per formula unit. Upon cooling, the $\chi_M T$ product exhibits a gradual decrease and then falls to a minimum value of 0.41 $cm^3\cdot mol^{-1}\cdot K$ for **1b** and 0.07 $cm^3\cdot mol^{-1}\cdot K$ for **1c**, as a result of the depopulation of the ground J multiplet split by the crystal field and intermolecular antiferromagnetic interactions between Ln^{3+} ions [69-70]. The plot of χ_M^{-1} versus T over the entire temperature range (Fig. S15) is well described by the Curie–Weiss law with Curie constant C = 0.85 $cm^3\cdot mol^{-1}\cdot K$ for **1b** and 1.89 $cm^3\cdot mol^{-1}\cdot K$ for **1c**, and Weiss constant θ = -17.73 K for **1b** and -54.55 K for **1b**, which also confirms the occurrence of antiferromagnetic exchange interactions between the Ln^{3+} centers.

For **2a-b**, $\chi_M T$ values at 300 K are equal to 3.29 $cm^3\cdot mol^{-1}\cdot K$ for **2a** and 23.04 $cm^3\cdot mol^{-1}\cdot K$ for **2b**, these values are as expected for two magnetically isolated Ln^{3+} ions (3.28 $cm^3\cdot mol^{-1}\cdot K$ for Nd^{3+}, $^4I_{9/2}$, S = 3/2, L = 6, g = 8/11, J = 9/2, and 22.74 $cm^3\cdot mol^{-1}\cdot K$ for Er^{3+}, $^4I_{15/2}$, S = 3/2, L = 6, J = 15/2, g = 6/5). For **2a**, as the temperature decreases, the $\chi_M T$ shows a gradual decrease, reaching 1.89 $cm^3\cdot mol^{-1}\cdot K$ at 2.0 K. For **2b**, upon cooling, the $\chi_M T$ remains practically constant until 100 K and it decreases further to reach a value of 10.52 $cm^3\cdot mol^{-1}\cdot K$ at 2 K. The plots of **2a-b** are indicative of the existence of a weak antiferromagnetic coupling between the Ln^{3+} ions. Antiferromagnetic interactions between Ln^{3+} ions of **2a-b** can be also confirmed by the smaller

Ln–O–Ln angle value (104.93(7) ° for **2a** and 105.75(8) ° for **2b**), because the rule is that Ln–O–Ln angles below 113.50 ° are assumed to cause an antiferromagnetic exchange in the literature [71-74]. The χ_M^{-1} versus T over the entire temperature range for **2a**-**b** can be fitted to the Curie–Weiss law, $\chi_M = C/(T-\theta)$ with the Curie constant C = 3.34 and 23.46 $cm^3 \cdot mol^{-1} \cdot K$, and the Weiss constant θ = −22.24 and −6.08 K, respectively (Fig. S15).

For **3**, the $\chi_M T$ value of 0.57 $cm^3 \cdot mol^{-1} \cdot K$ at 300 K is much higher than the expected value for two magnetically isolated Sm^{3+} ions (0.18 $cm^3 \cdot mol^{-1} \cdot K$ for Sm^{3+}, $^6H_{5/2}$, S = 5/2, L = 5, g = 2/7, J = 5/2) per formula unit, because not only the ground state but also the first exited state ($^6H_{7/2}$) and above for the Sm^{3+} ion can be populated at room temperature [75-77]. Upon cooling, the $\chi_M T$ value decreases rapidly, which could result from thermal depopulation of the excited-state levels. The χ_M^{-1} versus T for **3** does not obey the Curie–Weiss law that could result from spin–orbit coupling splits of the $^6H_{5/2}$ ground state [78].

For **4** and **5**, the $\chi_M T$ at 300 K are 15.28 $cm^3 \cdot mol^{-1} \cdot K$ for **4** and 23.73 $cm^3 \cdot mol^{-1} \cdot K$ for **5**, which are close to the theoretical value for two magnetically isolated Ln^{3+} ions (15.75 $cm^3 \cdot mol^{-1} \cdot K$ for Gd^{3+}, $^8S_{7/2}$, S = 7/2, L = 0, J = 7/2, g = 2, and 13.64 $cm^3 \cdot mol^{-1} \cdot K$ for Tb^{3+}, $^7F_6$, S = 3, L = 3, J = 6, g = 3/2). Upon cooling, the observed $\chi_M T$ product gradually decreases, and then drops to a minimum value of 11.05 $cm^3 \cdot mol^{-1} \cdot K$ for **4** and 12.04 $cm^3 \cdot mol^{-1} \cdot K$ for **5** at 2 K as a consequence of the depopulation of sublevels of the ground J multiplet split by the crystal field and intermolecular antiferromagnetic interactions. For **4**, the *anti-anti*–COO bridge within the dimeric entity appears as the most likely pathways for the antiferromagnetic exchange [5]. For **5**, the Tb–O–Tb angle value of 105.42 ° is significantly smaller than 113.50 ° [71-74], which is further confirmed the occurrence of antiferromagnetic exchange interactions between the Tb^{3+} ions. The χ_M^{-1} versus T over the entire temperature range for **2a**-**b** can be fitted to the Curie–Weiss law with C = 15.21 and 23.97 $cm^3 \cdot mol^{-1} \cdot K$ and θ = −1.66 and −5.03 K, respectively. The negative sign of θ also indicates a relatively weak local antiferromagnetic interaction between Ln^{3+} ions.

Conclusions

Although some transition metal azelates were obtained by the reaction of different transition metal ions and H_2aze ligands, no lanthanide azelates have been documented to date. Therefore, this work offers the only example of lanthanide azelates. Moreover, the reported transition metal azelates usually show the neutral extended frameworks, but their cationic

extended frameworks have been observed in **4** and **5**. **2a-b** exhibit interesting NIR luminescence, while **5** exhibits excellent luminescent sensor targeted for Fe^{3+} ion, due to the presence of the free $Hphen^{+}$ ion. **2a-b** and **3-5** exhibit stronger characteristic Ln^{3+} emissions, due to the incorporation of phen chromophores into lanthanide azelate frameworks. The successful syntheses of these lanthanide azelates enrich metal azelate family, and it is also expected that more novel lanthanide azelates with useful luminescent and magnetic properties might be synthesized by the combination of H_2aze liand and different π–conjugated aromatic chromophore.

Supplementary Information (SI) available:

Crystal data in CIF format can be obtained from the Web. The CIF table can be obtained free of charge via http://www.ccdc.cam.ac.uk/conts/retrieving.html, or from the Cambridge Crystallographic Data Centre, 12 Union Road, Cambridge CB2 1EZ, UK; fax: (+44) 1223-336-033; or e-mail: deposit@ccdc.cam.ac.uk. Supplementary data associated with this article can be found, in the online version.

Acknowledgment.

This work was supported by the NNSF of China (No. 21671029), the NSF of Chongqing (No. cstc2018jcyjAX0157), Program for leading talents of scientific and technological innovation in Chongqing (No. CSTCCXLJRC201707), and the Innovation Program for Chongqing's Overseas Returnees (No. cx2019037). This work was also developed within the scope of the project CICECO-Aveiro Institute of Materials, UIDB/50011/2020 & UIDP/50011/2020, financed by national funds through the Foundation for Science and Technology/MCTES.

References

[1] Yang X, Jones RA, Huang S. Luminescent 4f and d-4f polynuclear complexes and coordination polymers with flexible salen-type ligands. Coord Chem Rev 2014; 273-274: 63-75.

[2] Zheng S, Yang G. Recent advances in paramagnetic-TM-substituted polyoxometalates (TM= Mn, Fe, Co, Ni, Cu). Chem Soc Rev 2012; 41(22): 7623-46.

[3] Zheng X, Kong X, Zheng Z, Long L, Zheng L. High-nuclearity lanthanide-containing clusters as potential molecular magnetic coolers. Acc Chem Res 2018; 51(2): 517-25.

[4] Carlucci L, Ciani G, Proserpio DM, Mitina TG, Blatov VA. Entangled two-dimensional coordination networks: a general survey. Chem Rev 2014; 114(15): 7557-80.

[5] Zheng Y, Zheng Z, Chen X. A symbol approach for classification of molecule-based magnetic materials exemplified by coordination polymers of metal carboxylates. Coord Chem Rev 2014; 258-259: 1-15.

[6] Carlos LD, Ferreira RAS, Bermudez VZ, Julián-López B, Escribano P. Progress on lanthanide-based organic–inorganic hybrid phosphors. Chem Soc Rev 2011; 40(2): 536-49.

[7] Bünzli J-CG. Lanthanide luminescence for biomedical analyses and imaging. Chem Rev 2010; 110(5): 2729-55.

[8] Moore EG, Samuel APS, Raymond KN. From antenna to assay: lessons learned in lanthanide luminescence. Acc Chem Res 2009; 42(4): 542-52.

[9] Cui Y, Chen B, Qian G. Lanthanide metal-organic frameworks for luminescent sensing and light-emitting applications. Coord Chem Rev 2014; 273–274: 76-86.

[10] Binnemans K. Lanthanide-based luminescent hybrid materials. Chem Rev 2009; 109(9): 4283-374.

[11] Weissman SI. Intramolecular Energy Transfer The Fluorescence of Complexes of Europium. J Chem Phys 1942; 10(4): 214-7.

[12] Steemers FJ, Verboom W, Reinhoudt DN, van der Tol EB, Verhoeven JW. New Sensitizer-Modified Calix[4]arenes Enabling Near-UV Excitation of Complexed Luminescent Lanthanide Ions. J Am Chem Soc 1995; 117(37): 9408-14.

[13] Xu H, Liu F, Cui Y, Chen B, Qian G. A luminescent nanoscale metal–organic framework for sensing of nitroaromatic explosives. Chem Commun 2011; 47(11): 3153-5.

[14] Rieter WJ, Taylor KML, Lin W. Surface Modification and Functionalization of Nanoscale Metal-Organic Frameworks for Controlled Release and Luminescence Sensing. J Am Chem Soc 2007;129(32):9852–3.

[15] Chen B, Yang Y, Zapata F, Lin G, Qian G, Lobkovsky EB. Luminescent Open Metal Sites within a Metal–Organic Framework for Sensing Small Molecules. Adv. Mater. 2007; 19(13):1693–6.

[16] Hanaoka K, Kikuchi K, Kojima H, Urano Y, Nagano T. Selective Detection of Zinc Ions with Novel Luminescent Lanthanide Probes. Angew Chem 2003; 115(26): 3104–7.

[17] Chen B, Wang L, Zapata F, Qian G, Lobkovsky E B. A Luminescent Microporous Metal−Organic Framework for the Recognition and Sensing of Anions. J Am Chem Soc 2008; 130(21): 6718–9.

[18] Cui Y, Xu H, Yue Y, Guo Z, Yu J, Chen Z, Gao J, Yang Y, Qian G, Chen B. A Luminescent Mixed-Lanthanide Metal–Organic Framework Thermometer. J Am Chem Soc 2012; 134(9): 3979–82.

[19] Hasegawa Y, Kitagawa Y. Thermo-sensitive luminescence of lanthanide complexes, clusters, coordination polymers and metal–organic frameworks with organic photosensitizers. J Mater Chem C 2019; 7(25): 7494−511.

[20] Liu L, Qiu X, Wang Y, Shi Q, Sun Y, Chen Y. NIR emission and luminescent sensing of lanthanide-organic framework with Lewis basic imidazole and pyridyl sites. Dalton Trans 2017; 46(36): 12106−13.

[21] Sun Y, Wan F, Li X, Lin J, Wu T, Zheng S, Bu X. A lanthanide complex for metal encapsulations and anion exchanges. Chem Commun 2016; 52(66): 10125–8.

[22] Ding L, Liu L, Shi Q, Sun Y, Wang Y, Chen Y. Luminescent 3D Lanthanide–Cadmium Heterometal–Organic Frameworks with Chemical Stability and Selective Luminescent Sensing. Inorg Chem 2017; 56(24): 14850−8.

[23] Martinez JL. Environmental pollution by antibiotics and by antibiotic resistance determinants. Environ Pollut 2009;157(11):2893-902.

[24] Bricks JL, Kovalchuk A, Trieflinger C, Nofz M, Büschel M, Tolmachev AI, Daub J, Rurack K. On the Development of Sensor Molecules that Display Fe^{III}-amplified Fluorescence. J Am Chem Soc 2005; 127(39): 13522-9.

[25] Hyman LM, Franz KJ. Probing oxidative stress: Small molecule fluorescent sensors of metal ions, reactive oxygen species, and thiols. Coord Chem Rev 2012; 256(19-20): 2333-56.

[26] Xu XY, Yan B. Eu(III)-Functionalized MIL-124 as Fluorescent Probe for Highly Selectively Sensing Ions and Organic Small Molecules Especially for Fe(III) and Fe(II). ACS Appl Mater Interfaces 2015; 7(1): 721-9.

[27] Zheng M, Tan H, Xie Z, Zhang L, Jing X, Sun Z. Fast Response and High Sensitivity Europium Metal Organic Framework Fluorescent Probe with Chelating Terpyridine Sites for Fe^{3+}. ACS Appl Mater Interfaces 2013; 5(3): 1078-83.

[28] Zhao X, Tian D, Gao Q, Sun H, Xu J, Bu X. A chiral lanthanide metal-organic framework for selective sensing of Fe(III) ion. Dalton Trans 2016; 45(3): 1040-6.

[29] Xu H, Hu H, Cao C, Zhao B. Lanthanide Organic Framework as a Regenerable Luminescent Probe for Fe^{3+}. Inorg Chem 2015; 54(10: 4585-7.

[30] Sun Y, Wan F, Li X, Lin J, Wu T, Zheng S, Bu X. A lanthanide complex for metal encapsulations and anion exchanges. Chem Commun 2016; 52(66): 10125-8.

[31] Liu L, Qiu X, Wang Y, Shi Q, Sun Y, Chen Y. NIR emission and luminescent sensing of a lanthanide–organic framework with Lewis basic imidazole and pyridyl sites. Dalton Trans 2017; 46(36): 12106-13.

[32] Dang S, Ma E, Sun Z, Zhang H. A layer-structured Eu-MOF as a highly selective fluorescent probe for Fe^{3+} detection through a cation-exchange approach. J Mater Chem 2012; 22(33): 16920-6.

[33] Puntus LN, Lyssenko KA, MY Antipin, Bünzli JG. Role of inner-and outer-sphere bonding in the sensitization of Eu^{III}-luminescence deciphered by combined analysis of experimental electron density distribution function and photophysical data. Inorg Chem 2008; 47(23): 11095-107.

[34] (b) Ma X, Li X, Cha Y, Jin L. Highly thermostable one-dimensional lanthanide (III) coordination polymers constructed from benzimidazole-5, 6-dicarboxylic acid and 1, 10-phenanthroline: synthesis, structure, and tunable white-light emission. Cryst Growth Des 2012; 12(11): 5227-32.

[35] Biju S, Ambili Raj DB, Reddy MLP, Kariuki BM. Synthesis, crystal structure, and luminescent properties of novel Eu^{3+} heterocyclic β-diketonate complexes with bidentate nitrogen donors. Inorg Chem 2006; 45(26): 10651-60.

[36] D'Vries RF, Gomez GE, Lionello DF, Fuertes MC, Soler-Illia GJAA, Ellena J. Luminescence, chemical sensing and mechanical properties of crystalline materials based on lanthanide–sulfonate coordination polymers. RSC Adv 2016; 6(111): 110171-81.

[37] Tan X, Zhou J, Zou H, Fu L, Tang Q. A Series of Lanthanide–Germanate Oxo Clusters Decorated by 1,10-Phenanthroline Chromophores. Inorg Chem 2017; 56(17): 10361-9.

[38] Tan X, Zhou J, Zou H, Fu L, Tang Q, Wang P. A series of lanthanide glutarates: lanthanide contraction effect on crystal frameworks of lanthanide glutarates. RSC Adv 2017; 7(29): 17934-40.

[39] Liu X, Zhou J, Zou H, Fu L. A 2-D dysprosium glutarate exhibiting slow magnetic relaxation and luminescent properties. J Coord Chem 2018; 71(16-18): 2722-31.

[40] Jiang T, Zhou J, Li R, Zou H, Fu L. The only examples of cationic lanthanide pimelate frameworks decorated by π-conjugated 1, 10-phenanthrolines. Inorg Chim Acta 2018; 471: 377-83.

[41] Han L, Zhang X, Chen J, Li Z, Sun D, Wang X, Sun D. Silver (I)/Bipyrazole/Dicarboxylate Interpenetrated Coordination Networks: Spontaneous Chiral Resolution, Modulation of Topologies, Water Clusters, and Photoluminescences. Cryst Growth Des 2014; 14(5): 2230-9.

[42] Zhao F, Che Y, Zheng J. Unprecedented 3D host-framework based on a Ni_5 cluster with helical chains as guest: synthesis, structure, and magnetic property. Cryst Growth Des 2012; 12(10): 4712-5.

[43] Lin Y, Zhang Y, Zhang J, Chen X. Pillaring Zn-Triazolate Layers with Flexible Aliphatic Dicarboxylates into Three-Dimensional Metal-Organic Frameworks. Cryst Growth Des 2008; 8(10): 3673-9.

[44] Han L, Wang S, Jagličić Z, Zeng S, Zheng J, Li Z, Chen J, Sun D. Synthesis, structural versatility and magnetic properties of a series of copper (II) coordination polymers based on bipyrazole and various dicarboxylate ligands. CrystEngComm 2015; 17(6): 1405-15.

[45] Zheng Y, Lin J. Two heteroleptic Zinc (II) complexes:$[Zn(phen)(C_9H_{15}O_6)_2]$ and $[Zn_2(phen)_2(H_2O)_2(C_{10}H_{16}O_4)_2]\cdot 3H_2O$. Z Anorg Allg Chem 2003; 629(6): 1007-11.

[46] Zheng Y, Sun J, Lin J. An Azelaato‐bridged Dinuclear Copper (II) Complex, $[Cu_2(phen)_2(C_9H_{14}O_4)_2]\cdot 6H_2O$(phen=1,10-phenanthroline). Z. Anorg Allg Chem 2000; 626(6): 1271-3.

[47] Zhao F, Che Y, Zheng J. Three 3D complexes constructed from azelaic aci and rigid bis (imidazole) ligand: Syntheses, structures, thermal and photoluminescent properties. Inorg Chem Commun 2012; 24: 200-4.

[48] Sun D, Liu, F Hao H, Huang R, Zheng L. Different water clusters dependent on long-chain dicarboxylates in two Ag (I) coordination polymers: Synthesis, structure and thermal stability. J Mol Struct 2011; 1004(1-3): 313-8.

[49] Shyu E, Krishnan SM, Supkowski RM, LaDuca RL. Metal azelate coordination polymers containing a kinked dipyridyl tether: $CdSO_4$ topology and "ligand vacancy" primitive cubic three-dimensional networks. Polyhedron 2009; 28(8): 1437-46.

[50] Krishnan SM, Supkowski RM, LaDuca RL. One-and two-dimensional divalent copper coordination polymers based on kinked organodiimine and long flexible aliphatic dicarboxylate ligands. J Mol Struct 2008; 891(1-3): 423-8.

[51] Luo G, Zhu R, He W, Li M, Zhao Q, Li D, Dai J. Coexistence of cyclic $(CH_3OH)_2(H_2O)_8$ heterodecamer and acyclic water trimer in the channels of silver-azelate framework. J Mol Struct 2012; 1021: 84-8.

[52] Luo G, Wu D, Liu L, Xia J, Li D, Dai J, Xiao Z. A discrete water hexamer with a new planar tetrameric water moiety trapped in the crystal host of [Ag (azelate)(4, 4′-bipyridine)]·$(H_2O)_3$. J Mol Struct 2011; 1005(1-3): 172-7.

[53] Braga D, Giaffreda SL, Grepioni F. Solid-state preparation of hybrid organometallic–organic macrocyclic adducts with long chain dicarboxylic acids. Chem Commun 2006; 37: 3877-9.

[54] APEX3, SADABS, and SAINT, Bruker AXS Inc., Madison, WI, USA, 2008.

[55] Sheldrick GM. A short history of SHELX. Acta Crystallogr Sect A Found Crystallogr 2008; 64(1): 112-2.

[56] Benmerad B, Guehria-Laidoudi A, Balegroune F, Birkedal H, Chapuis G. Polymeric aqua (glutarato)(hydrogen glutarato) lanthanum(III) monohydrate. Acta Cryst 2000; C56(7): 789-92.

[57] Sushrutha SR, Natarajan S. Rare-earth carboxylates, $[Ln_2(III)(\mu_3\text{-}OH)(C_4H_4O_5)_2\text{-}(C_4H_2O_4)]\cdot 2H_2O$ [Ln = Ce, Pr and Nd]: synthesis, structure and properties. CrystEngComm 2014; 16(22): 4774-82.

[58] Zhou J, Zhao R, Yang T, Liu X, Xiao H, Zou H, Tan X. A series of new lanthanoid thioarsenates: insights into the influence of lanthanide contraction on the formation of new lanthanoid thioarsenates. Dalton Trans 2015; 44(16): 7203-12.

[59] Tan X, Zhou J, Fu L, Xiao H, Zou H, Tang Q. A series of new lanthanide fumarates displaying three types of 3-D frameworks. Dalton Trans 2016; 45(12): 5253-61.

[60] Zhao R, Zhou J, Liu X, Zhang L, Tang Q, Tan X. Solvothermal syntheses of lanthanide thiogermanates displaying three new structural moieties. RSC Adv 2014; 4(73): 38682-8.

[61] Wendlandt WW, Hecht HG. Reflectance Spectroscopy, Interscience Publishers, New York 1966.

[62] Zhou J. Synthesis of heterometallic chalcogenides containing lanthanide and group 13–15 metal elements. Coord Chem Rev 2016; 315: 112-34.

[63] Tang S, Zhou J, Zou H, Liu X, Zhang L. A Series of Lanthanide Selenidogermanates: The First Coexistence of Three Types of Selenidogermanate Units in the Same Architecture. Inorg Chem 2018; 57(3): 1242-50.

[64] An L, Zhou J, Zou H, Xiao H, Zhao R, Ding Q. Syntheses, structures and properties of a series of new lanthanide chalcoarsenates (III) containing crown-shaped $[As_3Q_6]^{3-}$ (Q = S, Se) clusters. J Alloy Compd 2017; 702: 594-600.

[65] Huang C. Rare Earth Coordination Chemistry, Fundamentals and Applications John Wiley & Sons, 2010.

[66] Li H, Liu Y, Liu J, Chen L, Zhao J, Yang G. Structural Transformation from Dimerization to Tetramerization of Serine-Decorated Rare-Earth-Incorporated Arsenotungstates Induced by the Usage of Rare-Earth Salts. *Chem Eur J* 2017; 23(11): 2673-89.

[67] Lakshminarayana G, Qiu J. Photoluminescence of Pr^{3+}, Sm^{3+} and Dy^{3+}: SiO_2–Al_2O_3–LiF–GdF_3 glass ceramics and Sm^{3+}, Dy^{3+}: GeO_2–B_2O_3–ZnO–LaF_3 glasses. Physica B 2009; 404(8-11): 1169-80.

[68] Hagan JJ, Taylor SC, Tweedle MF. Fluorescence Detection of Gadolinium Chelates Separated by Reversed-Phase High-Performance Liquid Chromatography. Anal. Chem. 1988, 60(6), 514-6.

[69] Wang Y-L, Ma Y, Yang X, Tang J-K, Cheng P, Wang Q-L, Li L-C, Liao D-Z. Syntheses, structures, and magnetic and luminescence properties of a new Dy^{III}-based single-ion magnet. Inorg Chem 2013; 52(13): 7380-6.

[70] Abbas G, Lan YH, Kostakis GE, Wernsdorfer W, Anson CE, Powell AK. Series of isostructural planar lanthanide complexes $[Ln^{III}_4(\mu_3\text{-}OH)_2(mdeaH)_2(piv)_8]$ with single molecule magnet behavior for the Dy_4 analogue. Inorg Chem 2010; 49(17): 8067-72.

[71] Kanamori J. Anisotropy and magnetostriction of ferromagnetic and antiferromagnetic materials. Rado G T, SuhlH, Eds. Magnetism, Vol. I. New York: Academic Press,1963; 127-203.

[72] Baggio R, Calvo R, Garland M T, Pena O, Perec M, Rizzi A. Gadolinium and Neodymium Citrates: Evidence for Weak Ferromagnetic Exchange between Gadolinium(III) Cations. Inorg Chem 2005; 44(24): 8979-87.

[73] Benmerad B, Aliouane K, Rahahlia N, Guehria-Laïdoudi A, Dahaoui S, Lecomte C. Studies of two lanthanide coordination polymers built up from dinuclear units. J Rare Earths 2013; 31(1): 85-93.

[74] Tan X, Zhou J, Fu L, Xiao H, Zou H, Tang Q. A series of new lanthanide fumarates displaying three types of 3-D frameworks. Dalton Trans 2016; 45(12): 5253-61.

[75] Kahn O. Molecular Magnetism. VCH: New York, 1993.

[76] Li X, Chen C, Xiao H, Wang A, Liu C, Zheng X, Gao L, Yang X, Fang S. Luminescent, magnetic and ferroelectric properties of noncentrosymmetric chain-like complexes composed of nine-coordinate lanthanide ions. Dalton Trans 2013; 42(43): 15317-25.

[77] Xu N, Wang C, Shi W, Yan S-P, Cheng P, Liao D-Z. Magnetic and Luminescent Properties of Sm, Eu, Tb, and Dy Coordination Polymers with 2-Hydroxynicotinic Acid. Eur J Inorg Chem 2011; 2011(15): 2387-93.

[78] Chen M, Li L, Chen Y, Chen L. In-Phase Alignments of Asymmetric Building Units in Ln_4GaSbS_9 (Ln= Pr, Nd, Sm, Gd-Ho) and Their Strong Nonlinear Optical Responses in Middle IR. J Am Chem Soc 2011; 133(12): 4617-24.

Table 1 Crystallographic data for all compounds.

	1a	**1b**	**1c**	**2a**
formula	$C_{18}H_{33}LaO_{10}$	$C_{18}H_{33}CeO_{10}$	$C_{18}H_{33}O_{10}Pr$	$C_{51}H_{60}N_4Nd_2O_{13}$
Fw	548.35	549.56	550.35	1225.51
crystal system	Monoclinic	Monoclinic	Monoclinic	Triclinic
space group	$P2_1/n$	$P2_1/n$	$P2_1/n$	P-1
a, Å	9.1449(6)	9.1037(4)	9.1305(4)	9.6080(19)
b, Å	8.7178(5)	8.6770(3)	8.6828(4)	12.252(3)
c, Å	27.3909(18)	27.2174(12)	27.2915(13)	12.866(3)
α,°	90	90	90	105.81(3)
β,°	94.810(2)	94.747(2)	94.6230(16)	101.51(3)
γ,°	90	90	90	111.26(3)
V, $Å^3$	2176.0(2)	2142.60(15)	2156.58(17)	1280.8(6)
Z	4	4	4	1
T, K	296(2)	293(2)	293(2)	293(2)
Calcd density,$Mg.m^{-3}$	1.675	1.704	1.695	1.589
F(000)	1112	1115	1120	618
2θ(max), deg	50.19	55.87	50.19	55.93
Total reflns collected	25129	66642	12881	29542
Unique reflns	3859	5137	3804	6106
No. of param	277	270	270	346
R1[I>2σ(I)]	0.0207	0.0325	0.0415	0.0255
wR2(all data)	0.0416	0.0525	0.0782	0.0592
GOOF on F^2	1.134	1.116	1.127	1.081
	2b	**3**	**4**	**5**
formula	$C_{51}H_{60}Er_2N_4O_{13}$	$C_{30}H_{41}N_2O_{10}Sm$	$C_{33}H_{30}ClGdN_4O_8$	$C_{78}H_{71}Cl_3N_{10}O_{21}Tb_2$
Fw	1271.55	740.02	803.31	1908.66
crystal system	Triclinic	Triclinic	Monoclinic	Monoclinic
space group	P-1	P-1	$P2_1/c$	$P2_1/c$
a, Å	9.537(5)	10.963(2)	12.026(2)	14.1296(6)
b, Å	12.170(6)	12.816(3)	13.717(3)	21.0888(10)
c, Å	12.713(6)	13.495(3)	20.116(4)	26.0287(12)
α,°	106.378(15)	109.10(3)	90	90
β,°	100.936(17)	106.41(3)	106.417(6)	90.3504(15)
γ,°	111.208(19)	105.87(3)	90	90
V, $Å^3$	1247.6(11)	1572.3(7)	3183.0(11)	7755.8(6)
Z	1	2	4	4
T, K	293(2)	293(2)	293(2)	296(2)
Calcd density,$Mg.m^{-3}$	1.692	1.562	1.676	1.635
F(000)	634	752	1604	3832
2θ(max), deg	55.82	50.20	50.20	50.20
Total reflns collected	28778	35997	69039	220315
Unique reflns	5939	5588	5651	13786
No. of param	346	398	425	1239
R1[I>2σ(I)]	0.0245	0.0209	0.0303	0.0445
wR2(all data)	0.0481	0.0488	0.0796	0.0957
GOOF on F^2	1.135	1.102	1.122	1.322

Figure captions

Fig. 1 (a) The asymmetric unit of **1a** with the labeling scheme. (b) Coordination environment of the La^{3+} ion. (c) 1-D chain built up from La^{3+} ions and aze^{2-} ligands. View of a 3-D structure of **1a** along the [100] (d) and [010] (e) directions.

Fig. 2 (a) Coordination environment of the Nd^{3+} ion. (b) 2-D $[Nd_2(aze)_3(phen)_2]_n$ layer in **2a**. (c) The sql topology of **2a**. (d) π–π stacking interactions. (e) View of the stacking mode for the layers in **2a**. All H atoms and free water molecules have been omitted for clarity.

Fig. 3 (a) Coordination environment of the Sm^{3+} ion. (b) 1-D neutral $[Sm(aze)(Haze)(phen)]_n$ chain. (c) The π–π stacking interactions between the 1-D chains. (d) The crystal packing diagram of **3**. All H atoms are omitted for clarity.

Fig. 4 (a) 1-D $[Gd(aze)(phen)_2^+]_n$ chain in **4**. (b) 1-D $[Tb(aze)(phen)_2^+]_n$ chain in **5**. The π–π stacking interactions between the 1-D $[Gd(aze)(phen)_2^+]_n$ (c) and $[Tb(aze)(phen)_2^+]_n$ (d) chains. The crystal packing diagrams of **4** (e) and **5** (f). All H atoms are omitted for clarity.

Fig. 5 UV/Vis absorption spectra of **1c**, **2a-b** and **3** at room temperature.

Fig. 6 The emission spectra of **2a** (a)**, 2b** (b), **3** (c), and **5** (d) at room temperature.

Fig. 7 a) Luminescent spectra of **5** dispersed into various 0.1 M MCl_x aqueous solution, b) luminescent intensities at 545 nm of **5** treated with various 0.1 M MCl_x aqueous solution, c) luminescent spectra of **5** suspensions with different concentration of $FeCl_3$, d) Stern–Volmer plot of **5** quenched by $FeCl_3$ aqueous solution.

Fig. 8 The plot of $\chi_M T$ versus T for **1b-c**, **2a-b** and **3-5**.

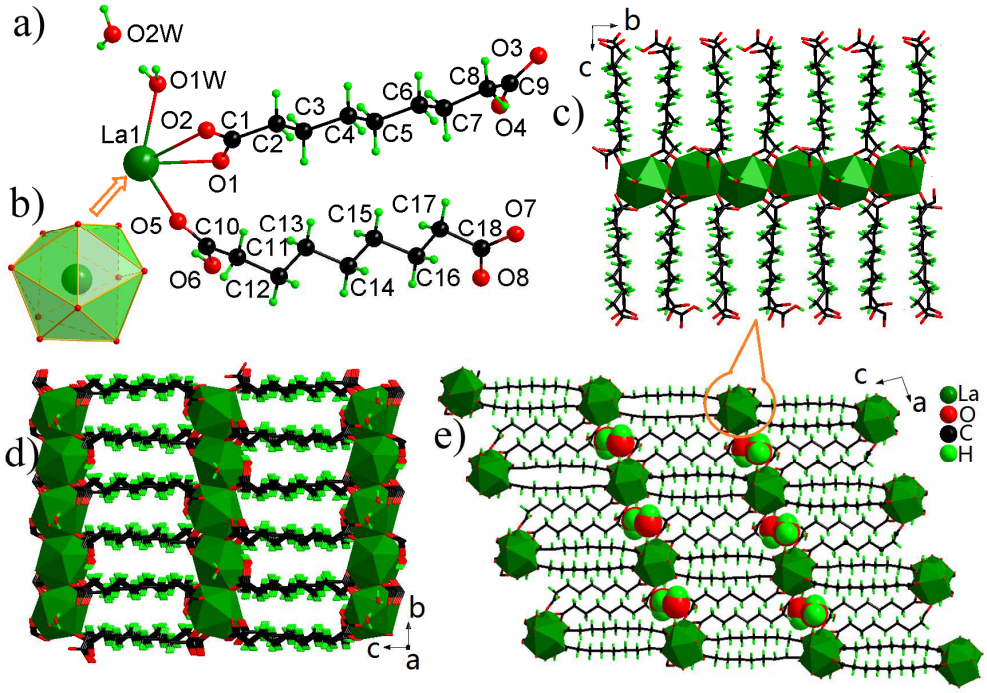

Fig. 1 (a) The asymmetric unit of **1a** with the labeling scheme. (b) Coordination environment of the La^{3+} ion. (c) 1-D chain built up from La^{3+} ions and aze^{2-} ligands. View of a 3-D structure of **1a** along the [100] (d) and [010] (e) directions.

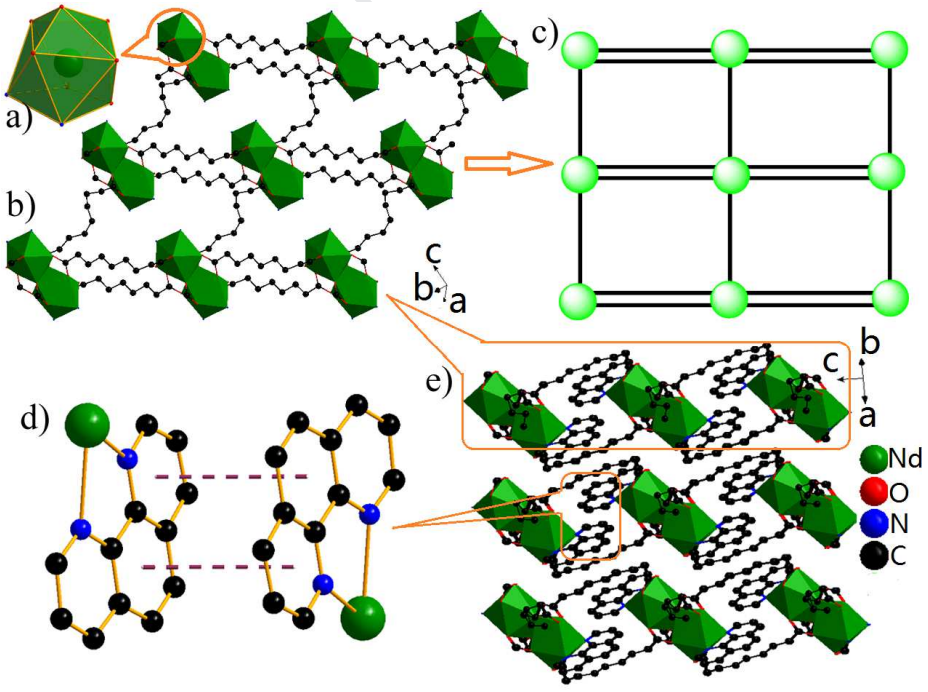

Fig. 2 (a) Coordination environment of the Nd^{3+} ion. (b) 2-D $[Nd_2(aze)_3(phen)_2]_n$ layer in **2a**. (c) The sql topology of **2a**. (d) π–π stacking interactions. (e) View of the stacking mode for the layers in **2a**. All H atoms and free water molecules have been omitted for clarity.

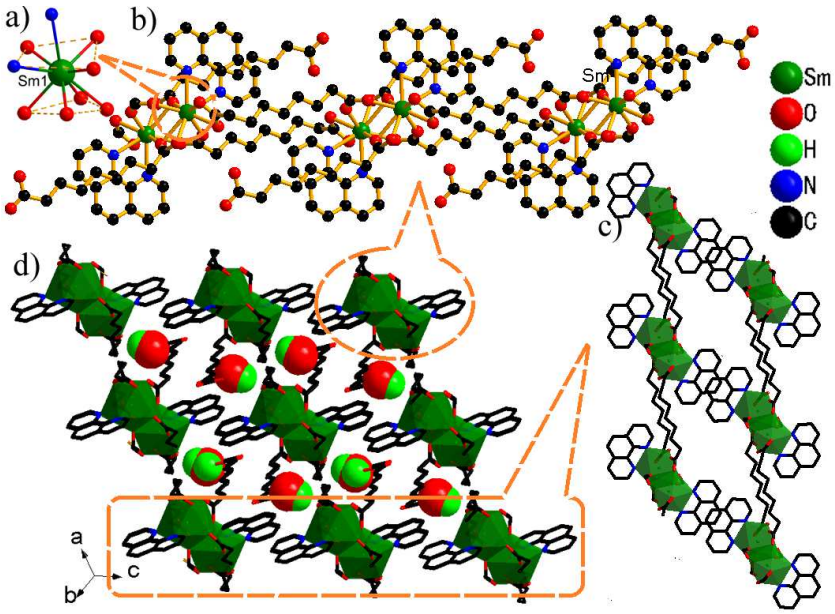

Fig. 3 (a) Coordination environment of the Sm^{3+} ion. (b) 1-D neutral $[Sm(aze)(Haze)(phen)]_n$ chain. (c) The π–π stacking interactions between the 1-D chains. (d) The crystal packing diagram of **3**. All H atoms are omitted for clarity.

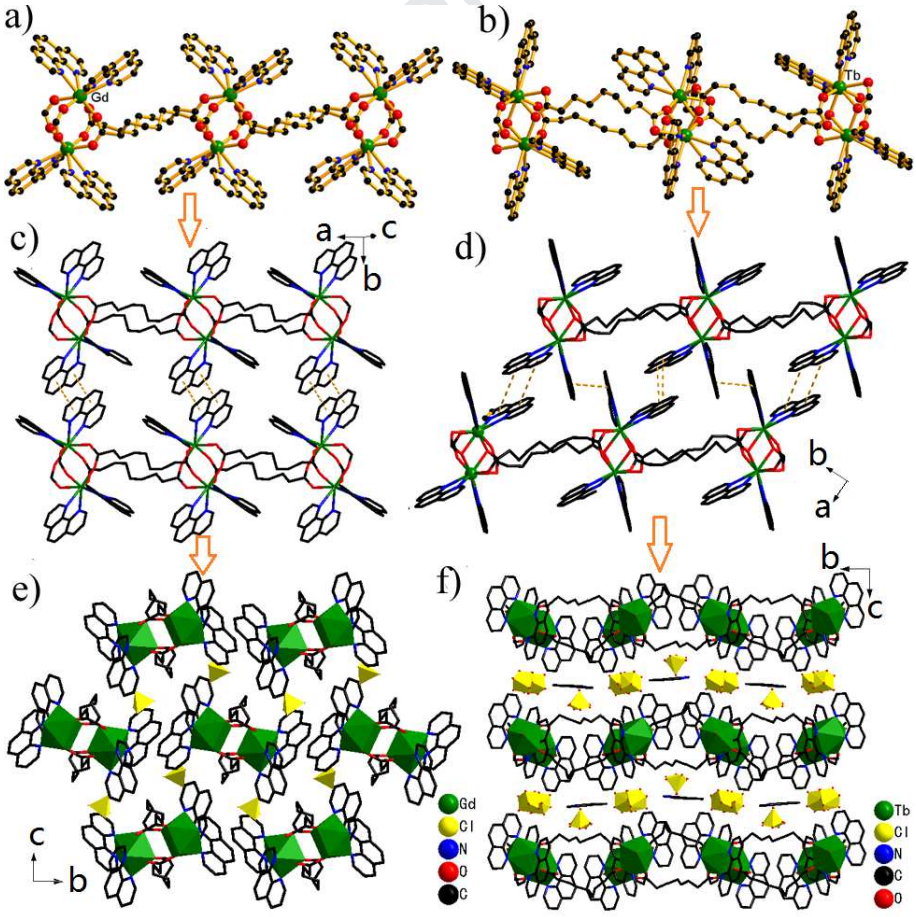

Fig. 4 (a) 1-D $[Gd(aze)(phen)_2^+]_n$ chain in **4**. (b) 1-D $[Tb(aze)\text{-}(phen)_2^+]_n$ chain in **5**. The π–π stacking interactions between the 1-D $[Gd(aze)(phen)_2^+]_n$ (c) and $[Tb(aze)(phen)_2^+]_n$ (d) chains. The crystal packing diagrams of **4** (e) and **5** (f). All H atoms are omitted for clarity.

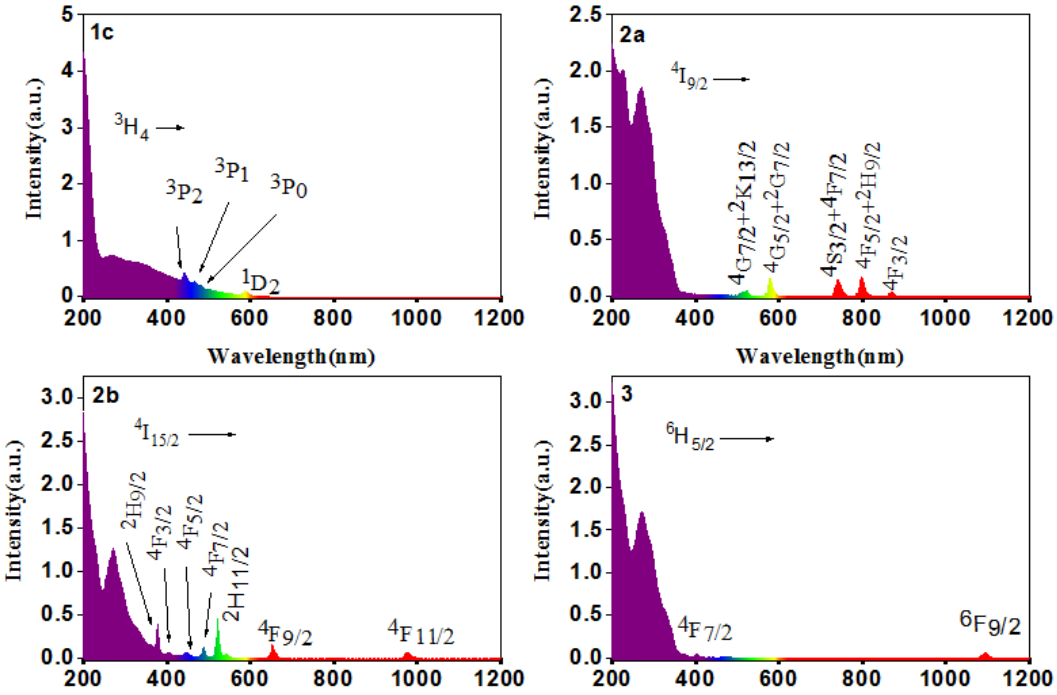

Fig. 5 UV/Vis absorption spectra of **1c**, **2a-b** and **3** at room temperature.

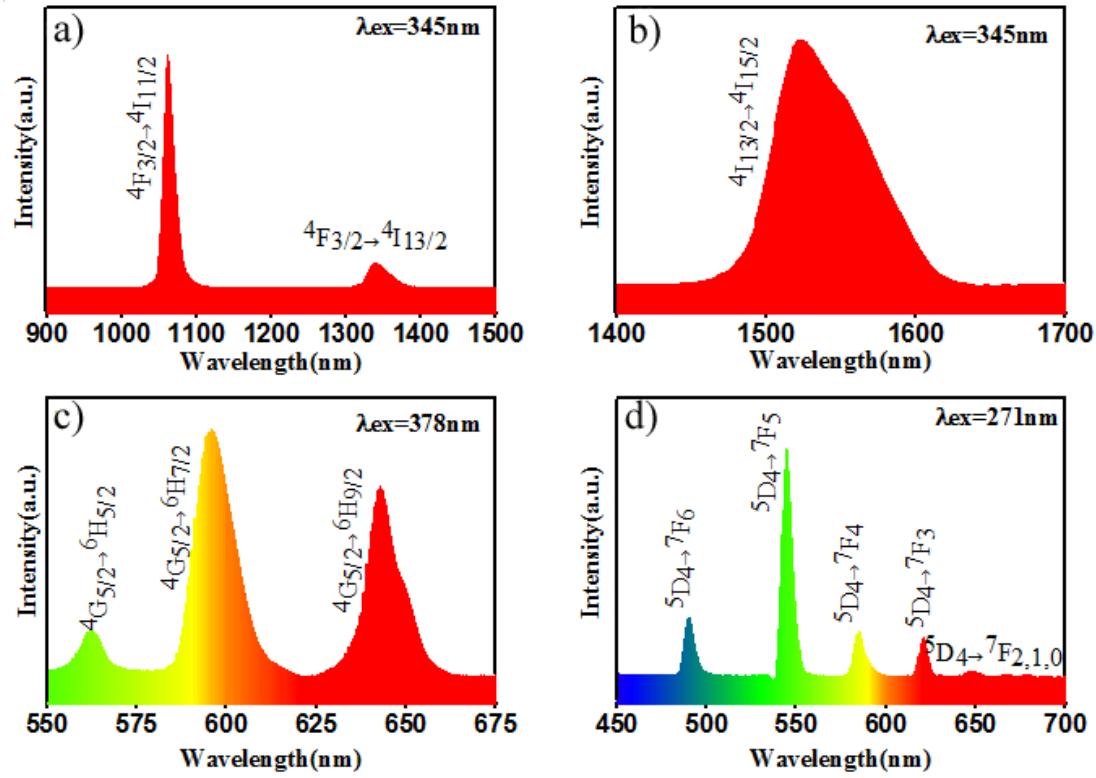

Fig. 6 The emission spectra of **2a** (a)**, 2b** (b), **3** (c), and **5** (d) at room temperature.

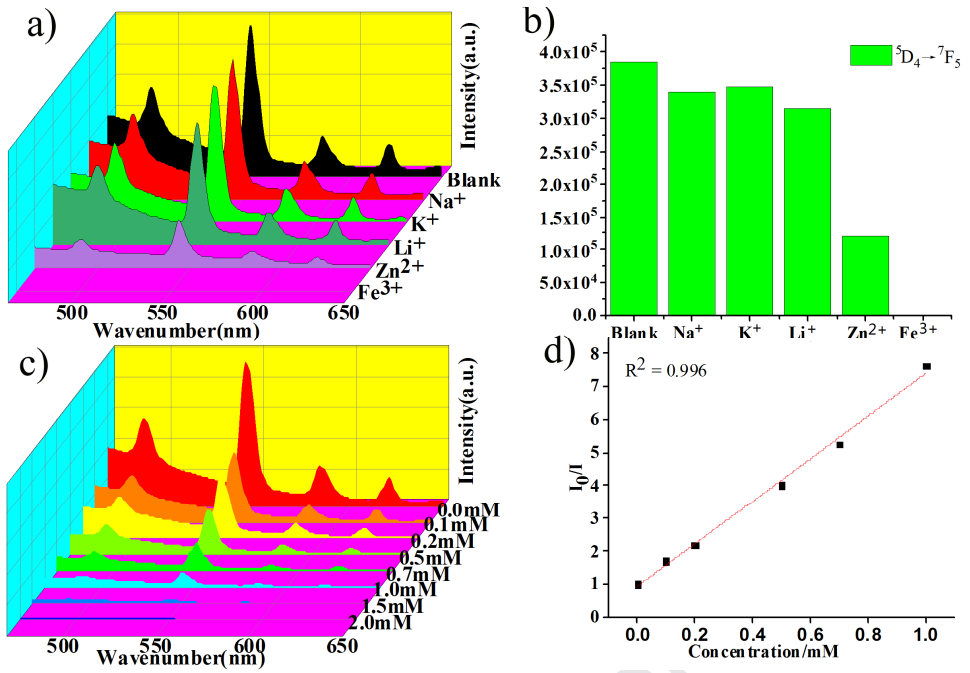

Fig. 7 a) Luminescent spectra of **5** dispersed into various 0.1 M MCl_x aqueous solution, b) luminescent intensities at 545 nm of **5** treated with various 0.1 M MCl_x aqueous solution, c) luminescent spectra of **5** suspensions with different concentration of $FeCl_3$, d) Stern–Volmer plot of **5** quenched by $FeCl_3$ aqueous solution.

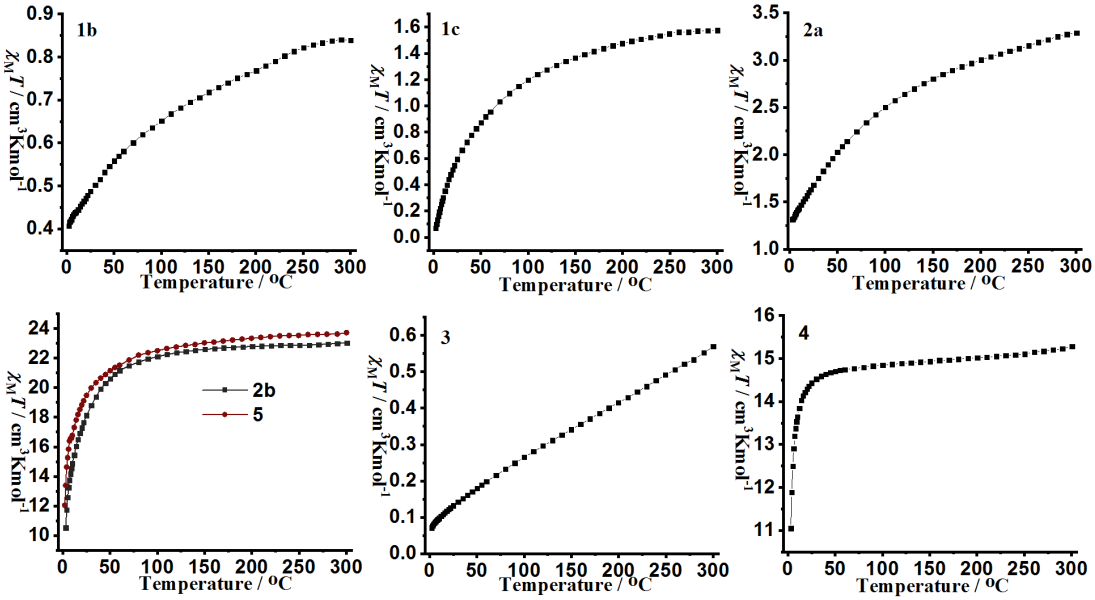

Fig. 8 The plot of $\chi_M T$ versus T for **1b-c**, **2a-b** and **3-5**.

Highlights: a) this work presents the only examples of lanthanide azelates exhibiting luminescent properties;

b) **2a**-**b** exhibit interesting NIR luminescence;

c) **5** shows excellent luminescent sensor targeted for Fe^{3+} ion;

d) **4**-**5** provide the only examples of cationic metal azelate frameworks.

Syntheses and luminescent properties of a series of new lanthanide azelates

Zhiwen Tan, Jian Zhou, Tingting Jiang, Hua-Hong Zou, and Lianshe Fu

Table S1. Ranges of Some Important Bond Distances(Å) and Bond Angles(°) for All Compounds

Bond	Dist(Å)	Angle	(°)
	1a		
La-O	2.4659(17)-2.7574(18)	O-La-O	48.58(6)-174.94(6)
	1b		
Ce-O	2.441(2)-2.755(2)	O-Ce-O	48.70(7)-144.87(8)
	1c		
Pr-O	2.429(4)-2.763(5)	O-Pr-O	48.56(14)-175.55(13)
	2a		
Nd-O	2.392(4)-2.635(4)	O-Nd-O	49.96(12)-146.06(14)
Nd-N	2.662(5)-2.679(5)	O-Nd-N	72.17(16)-147.71(15)
		N-Nd-N	61.69(15)
	2b		
Er-O	2.295(4)-2.429(5)	O-Er-O	53.80(15)-143.12(16)
Er-N	2.552(5)-2.593(5)	O-Er-N	68.70(16)-145.51(16)
		N-Er-N	63.38(16)
	3		
Sm-O	2.366(3)-2.486(3)	O-Sm-O	49.32(9)-148.59(10)
Sm-N	2.618(3)-2.687(4)	O-Sm-N	70.16(10)-146.17(10)
		N-Sm-N	70.16(10)
	4		
Gd-O	2.218(4)-2.273(3)	O-Gd-O	75.73(14)-125.91(13)
Gd-N	2.533(4)-2.551(4)	O-Gd-N	70.84(13)-146.96(14)
		N-Gd-N	64.47(13)-112.61(14)
	5		
Tb-O	2.306(6)-2.530(6)	O-Tb-O	72.1(2)-138.3(2)
Tb-N	2.578(7)-2.619(7)	O-Tb-N	64.2(2)-144.9(2)
		N-Tb-N	63.0(2)-123.7(2)

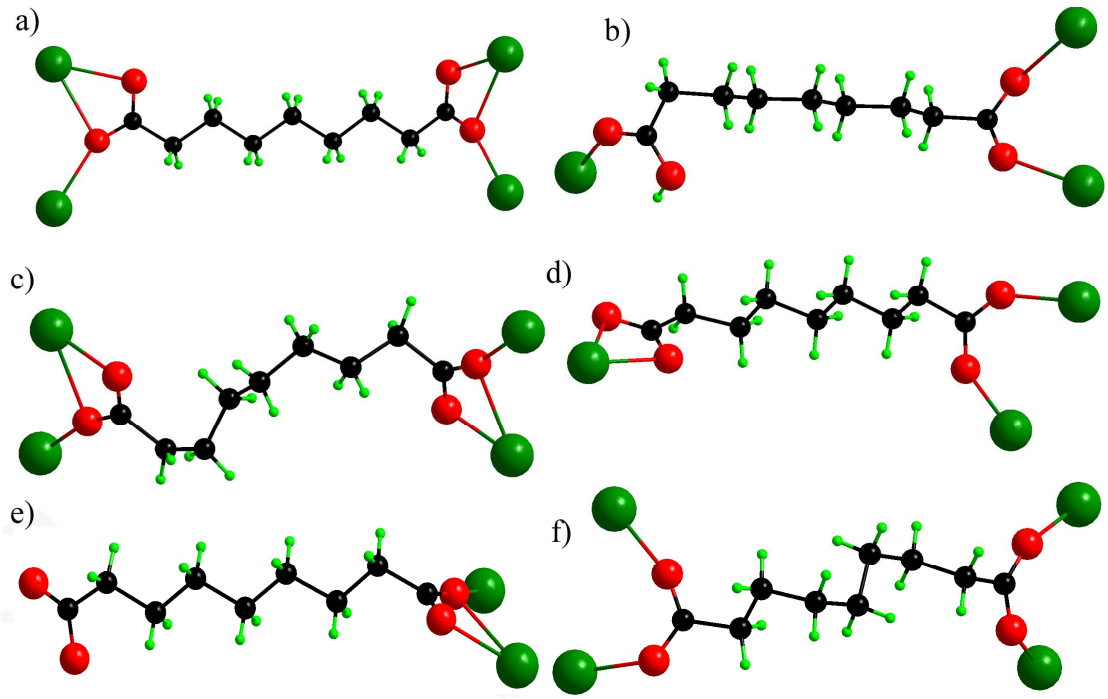

Fig. S1 The link modes of aze^{2-} or $Haze^{-}$ ligands.

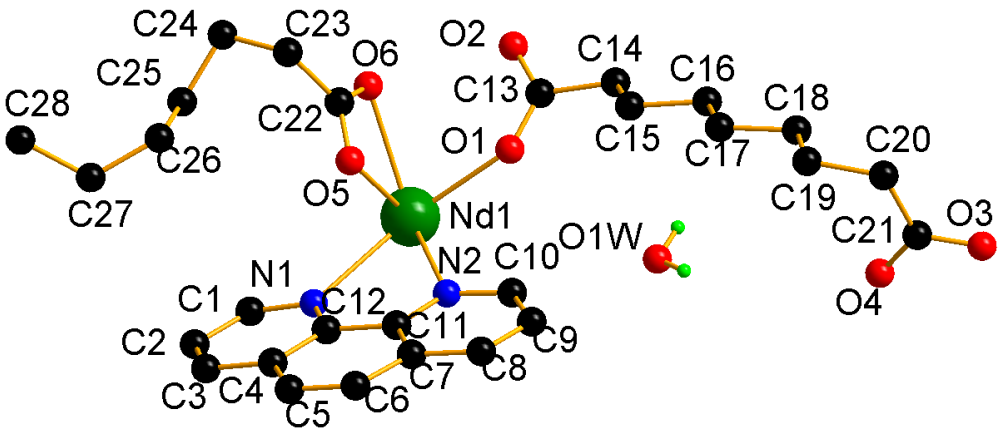

Fig. S2 The asymmetric unit of **2a** (H atoms bonded to C atoms have been omitted for clarity).

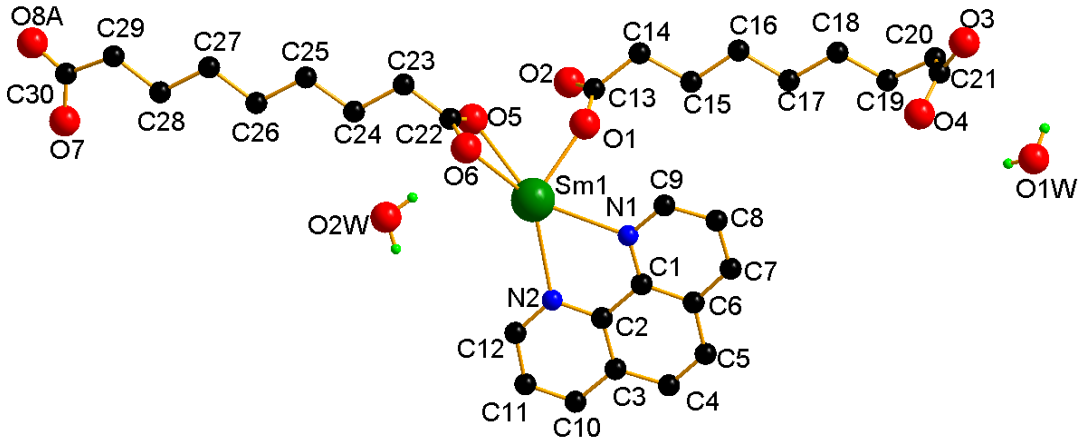

Fig. S3 The asymmetric unit of **3** (H atoms bonded to C atoms have been omitted for clarity).

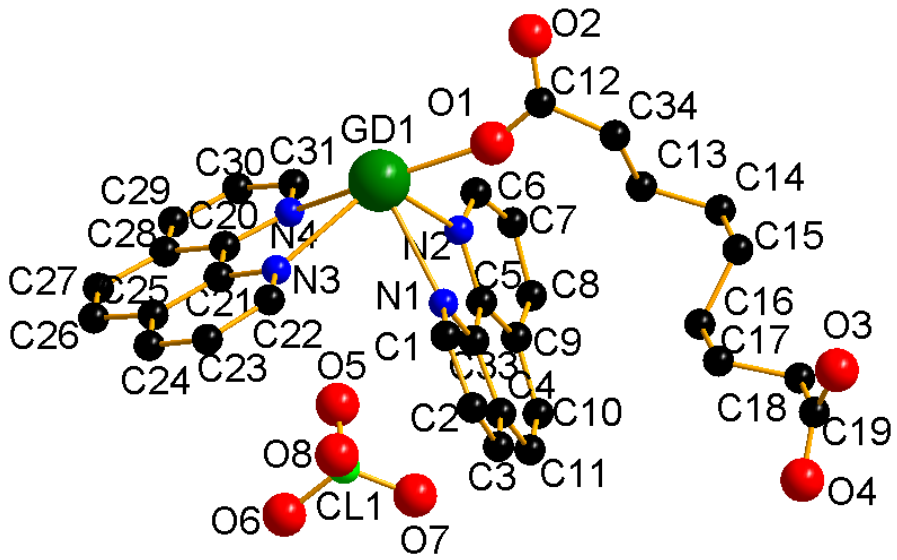

Fig. S4 The asymmetric unit of **4** (H atoms bonded to C atoms have been omitted for clarity).

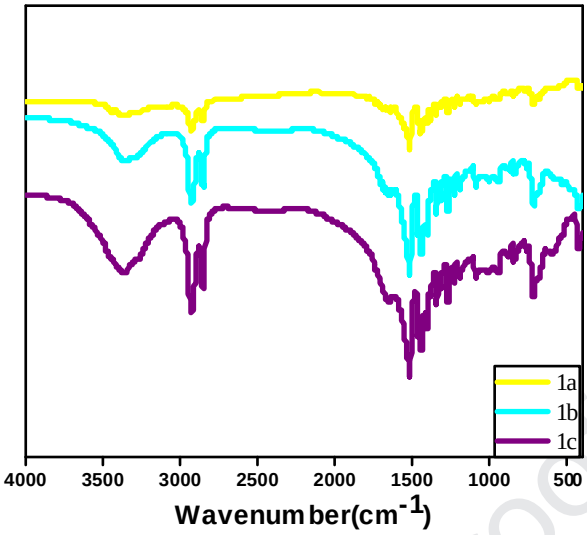

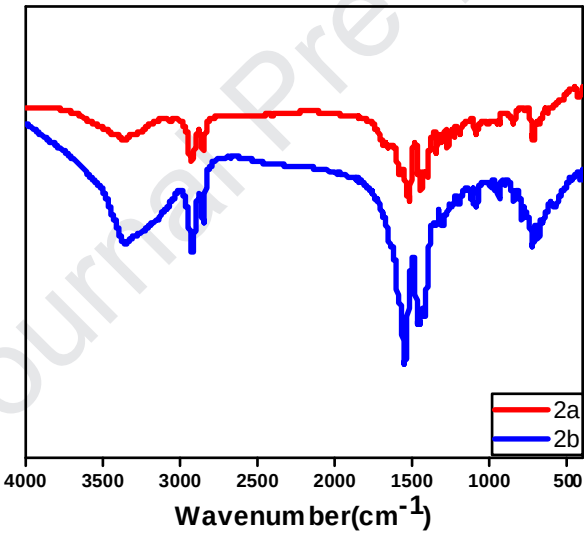

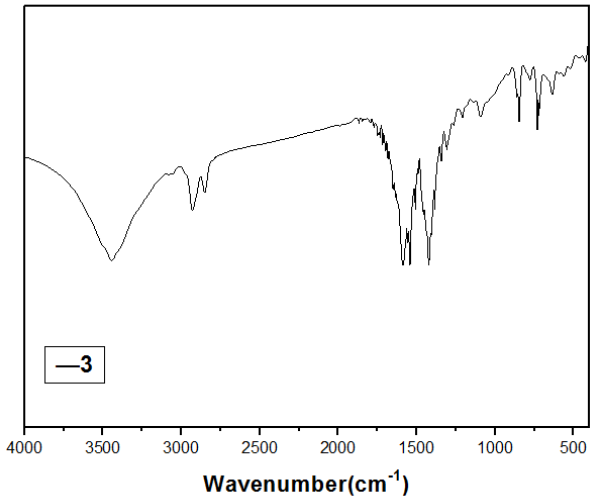

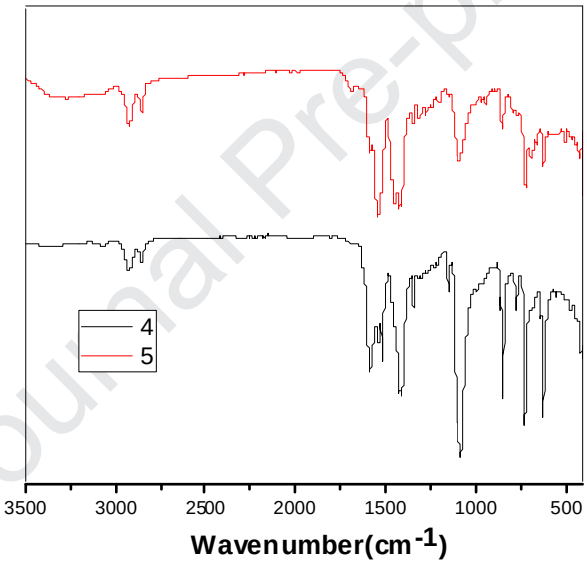

Fig. S5 The FTIR spectra of all compounds.

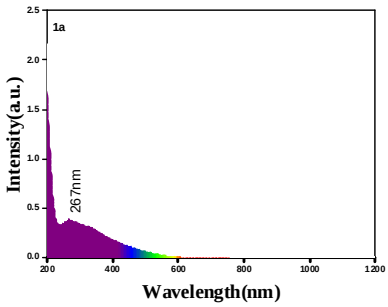

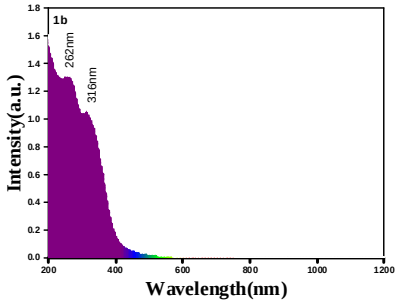

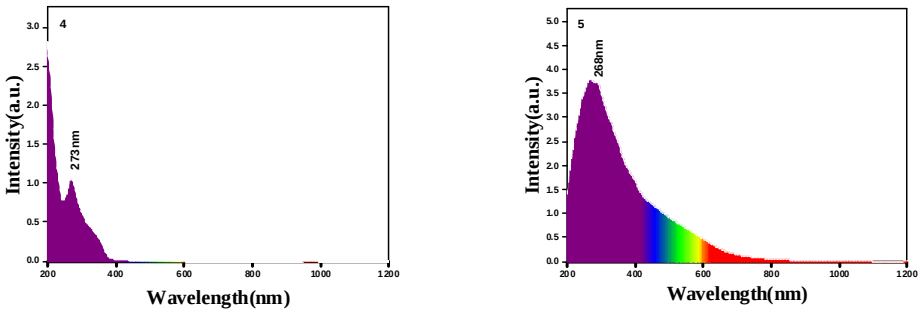

Fig. S6 UV/Vis absorption spectra of **1a-b**, **4** and **5** at room temperature.

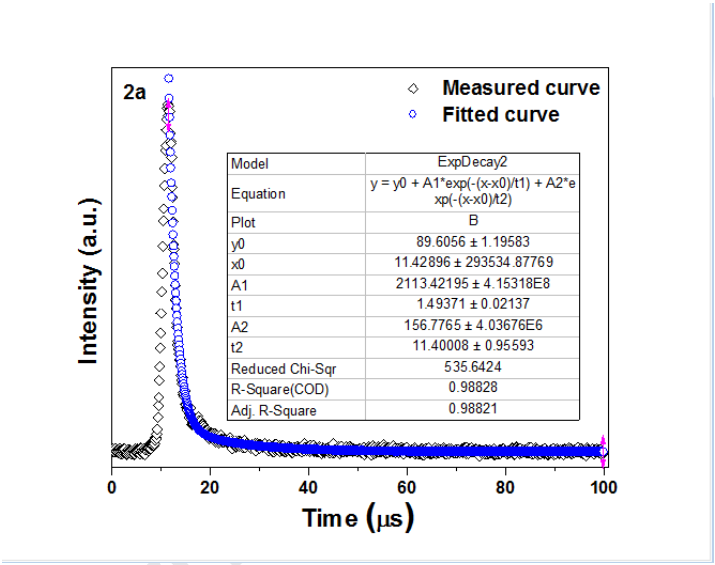

Fig. S7 The luminescence decay curve of **2a**.

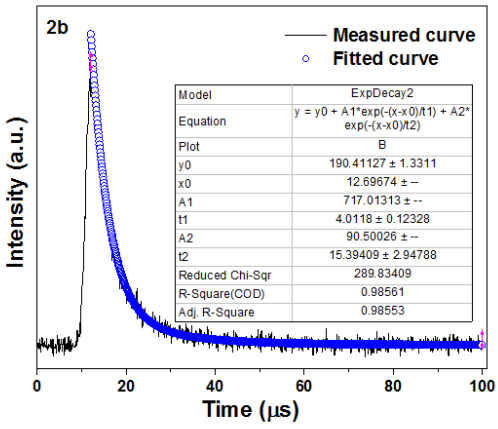

Fig. S8 The luminescence decay curve of **2b**.

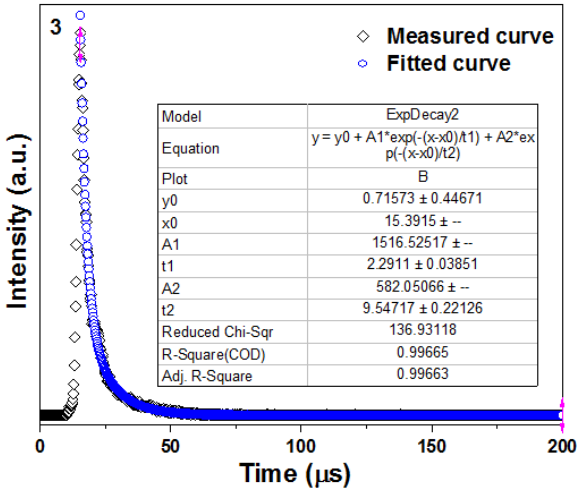

Model	ExpDecay2
Equation	y = y0 + A1*exp(-(x-x0)/t1) + A2*exp(-(x-x0)/t2)
Plot	B
y0	0.71573 ± 0.44671
x0	15.3915 ± --
A1	1516.52517 ± --
t1	2.2911 ± 0.03851
A2	582.05066 ± --
t2	9.54717 ± 0.22126
Reduced Chi-Sqr	136.93118
R-Square(COD)	0.99665
Adj. R-Square	0.99663

Fig. S9 The luminescence decay curve of **3.**

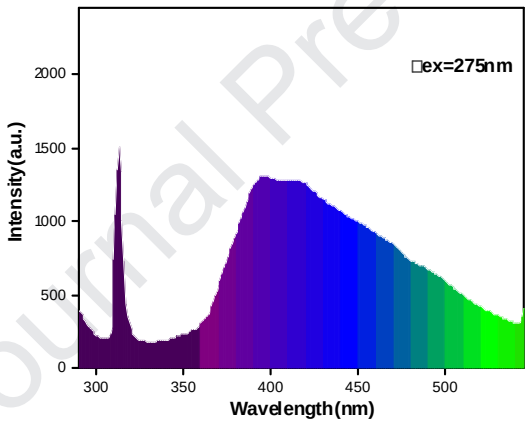

Fig. S10 the emission spectrum of **4**.

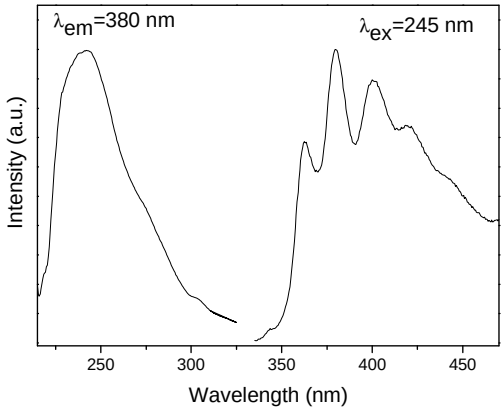

Fig. S11. Excitation (λ_{em}=380 nm) and emission (λ_{ex}=245 nm) spectra of phen.

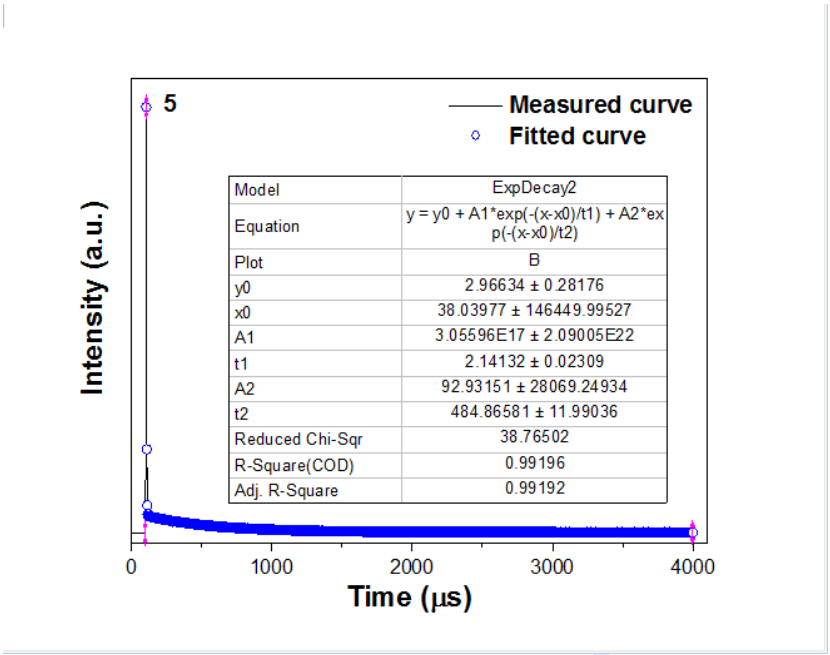

Fig. S12 The luminescence decay curve of **5.**

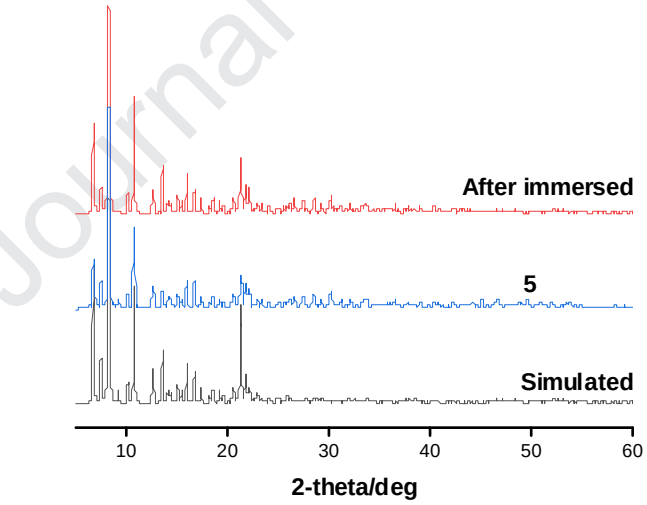

Fig. S13 Simulated, experimental and after immersed XRD patterns of **5**.

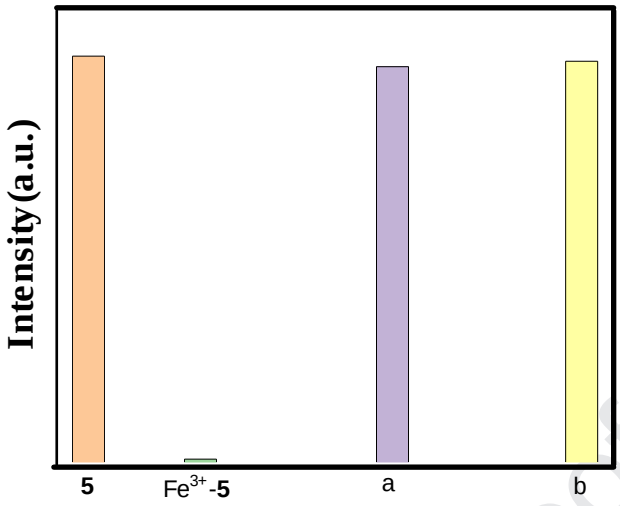

Fig. S14. The luminescence intensity (545 nm) of two recycles (a) after the first recycle, and (b) after the second recycle.

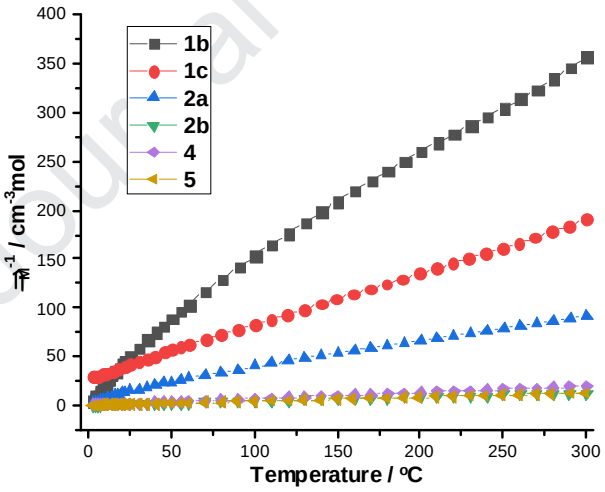

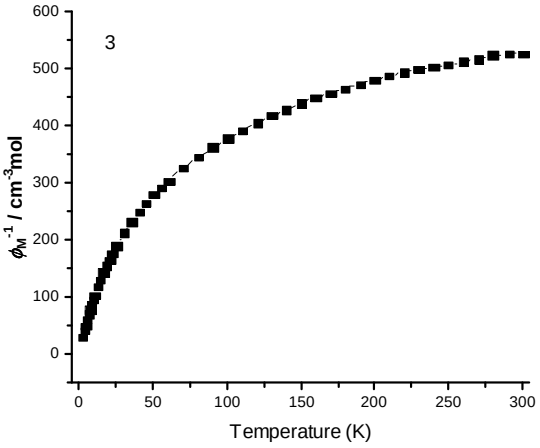

Fig. S15 The plot of χ_M^{-1} versus T for **1b-c**, **2a-b** and **3-5**.

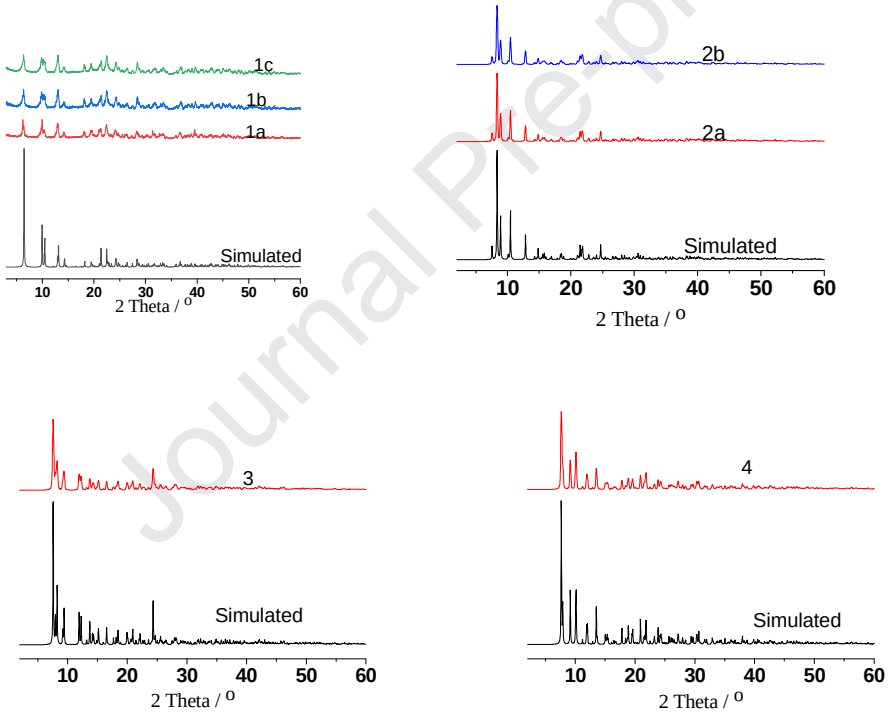

Fig. S16 Simulated and experimental powder XRD patterns of some compounds.

No Conflict of Interest Form.